DLG1 functions upstream of SDCCAG3 and IFT20 to control ciliary targeting of polycystin-2

Csenge K. Rezi[1], Mariam G. Aslanyan[2], Gaurav D. Diwan[3,4], Tao Cheng[5], Mohamed Chamlali[1], Katrin Junger[6], Zeinab Anvarian[1], Esben Lorentzen[7], Kleo B. Pauly[1], Yasmin Afshar-Bahadori[1], Eduardo F. A. Fernandes[8], Feng Qian[9], Sébastien Tosi[10], Søren T. Christensen[1], Stine F. Pedersen[1], Kristian Strømgaard[8], Robert B. Russell[3,4], Jeffrey H. Miner[5], Moe R. Mahjoub[5], Karsten Boldt[6], Ronald Roepman[2], Lotte B. Pedersen[1,*]

[1] Department of Biology, University of Copenhagen, Denmark

[2]Department of Human Genetics, Radboud Institute for Molecular Life Sciences, Radboud University Medical Center, Nijmegen, Netherlands

[3]BioQuant and [4]Biochemistry Center (BZH), Heidelberg University, Heidelberg, Germany

[5]Department of Medicine (Nephrology Division) and Department of Cell Biology and Physiology, Washington University, St Louis, MO, USA

[6]Institute for Ophthalmic Research, Eberhard Karl University of Tübingen, Tübingen, Germany

[7]Department of Molecular Biology and Genetics - Protein Science, Aarhus University, Denmark

[8]Center for Biopharmaceuticals, Department of Drug Design and Pharmacology, University of Copenhagen, Denmark

[9]Division of Nephrology, Department of Medicine, University of Maryland School of Medicine, Baltimore, MD, USA

[10]Danish BioImaging Infrastructure Image Analysis Core Facility (DBI-INFRA IACF), University of Copenhagen, Denmark

***Lead contact:** lbpedersen@bio.ku.dk

Keywords: DLG1, primary cilia, SDCCAG3, IFT20, retromer, polycystin-2, kidney epithelium, CAKUT

Summary

Polarized vesicular trafficking directs specific receptors and ion channels to cilia, but the underlying mechanisms are poorly understood. Here we describe a role for DLG1, a core component of the Scribble polarity complex, in regulating ciliary protein trafficking in kidney epithelial cells. Conditional knockout of *Dlg1* in mouse kidney caused ciliary elongation and cystogenesis, and cell-based proximity labelling proteomics and fluorescence microscopy showed alterations in the ciliary proteome upon loss of DLG1. Specifically, the retromer-associated protein SDCCAG3, IFT20 and polycystin-2 (PC2) were reduced in cilia of DLG1 deficient cells compared to control cells. This phenotype was recapitulated *in vivo* and rescuable by re-expression of wildtype DLG1, but not a Congenital Anomalies of the Kidney and Urinary Tract (CAKUT)-associated DLG1 variant, p.T489R. Finally, biochemical approaches and Alpha Fold modelling suggested that SDCCAG3 and IFT20 form a complex that associates, at least indirectly, with DLG1. Our work identifies a key role for DLG1 in regulating ciliary protein composition and suggests that ciliary dysfunction of the p.T489R DLG1 variant may contribute to CAKUT.

Introduction

Primary cilia are microtubule-based sensory organelles that protrude from the surface of many different vertebrate cell types, including kidney epithelial cells, and play essential roles in regulating various signalling pathways during embryonic development and adult homeostasis. Mutations in ciliary genes lead to deregulated signalling, in turn causing diseases known as ciliopathies. While dysfunctional cilia affect most organs in the body, renal involvement is a key feature of many ciliopathies [1]. For example, autosomal dominant polycystic kidney disease (ADPKD), one of the most common human monogenic diseases affecting ca. 1:1000 live births, can be caused by mutations in *PKD1* or *PKD2* encoding the cilium-localized transmembrane proteins polycystin-1 (PC1) and polycystin-2 (PC2), respectively, which form a heterodimeric calcium-permeable nonselective cation channel complex essential for tubular differentiation, polarity and diameter in the kidney [2-5].

Cilia are compartmentalized organelles that are thought to be devoid of protein synthesis machinery, and appropriate trafficking of PC1 and PC2, as well as other ciliary signalling receptors, ion channels and transporters, from their site of synthesis in the ER/Golgi to the ciliary compartment is essential for ciliary biogenesis and function. For example, a mutation that specifically impairs ciliary localization of PC2, one of the best studied ciliary ion channels, causes PKD in mice [6]. Additional studies have addressed the molecular mechanisms by which PC2 and other ciliary transmembrane proteins, such as G-protein coupled receptors (GPCRs), are sorted and transported from their site of synthesis in the ER/Golgi to the cilium. These studies have revealed a remarkable complexity and diversity in the mechanisms by which different transmembrane proteins are targeted and transported to the primary cilium [7-9]. In the case of PC2, studies of its glycosylation pattern indicated that PC2-containing vesicles destined to the cilium are initially released from the cis-Golgi compartment instead of the trans-Golgi network (TGN) [10, 11] although this was

questioned by others [12]. Regardless, it is believed that shortly after synthesis, PC2 interacts with the ciliary intraflagellar transport (IFT)-B complex subunit IFT20, which is anchored to the cis-Golgi compartment by golgin protein GMAP210/TRIP11, and facilitates the transport of PC2 to the base of the primary cilium [13, 14]. Following sorting at the cis-Golgi or TGN, PC2-containing vesicles are thought to be directed towards the plasma membrane or recycling endosomes before PC2 is delivered at the ciliary base where it docks at the transition fibers prior to being imported into the cilium [6, 7, 9]. Consistent with recycling endosomes playing a critical role in conferring PC2 targeting to the primary cilium, disruption of recycling endosome-associated proteins, such as retromer-associated proteins and the biogenesis of lysosome-related organelles complex 1 (BLOC-1) complex, or the Rab family small GTPases RAB8 and RAB11, reduces ciliary PC2 levels [7, 11, 15, 16]. Whether and how components located at the plasma membrane contribute to ciliary PC2 trafficking is largely unknown.

Discs large MAGUK scaffold protein 1 (DLG1) is a scaffold protein that belongs to the membrane-associated guanylate kinase homolog (MAGUK) family and is composed of a LIN-2,-7 (L27) domain, three postsynaptic density-95/discs large/zona occludens-1 (PDZ) domains, a SRC homology 3 (SH3) domain and a catalytically inactive guanylate kinase (GUK) domain. First described in *Drosophila*, this evolutionarily conserved scaffold protein is well known for its role in apical-basal polarity establishment and maintenance in epithelial cells, where it forms a complex with SCRIB and LGL at the basolateral membrane below the adherens junctions [17]. Consistent with its domain structure, the DLG1 interaction network is vast, and its function extends beyond epithelial cell polarity establishment. For instance, in neurons DLG1 localizes to both the presynaptic and postsynaptic membranes and controls localization and clustering of glutamate receptors and potassium channels by mediating interaction between receptors and intracellular proteins [18-22]. Several studies also

suggested that DLG1 localizes to the cilium-centrosome axis. Specifically, in HT1299 cells DLG1 was reported to localize to mitotic centrosomes in a PTEN-NEK6-Eg5 dependent manner [23], whereas three independent studies found DLG1 in the ciliary proteome of cultured mouse kidney inner medullary collecting duct 3 (IMCD3) cells [24, 25] and photoreceptor outer segments [26], which are modified primary cilia. DLG1 also binds directly to kinesin-3 motor KIF13B [27], which was shown previously to localize dynamically to the primary cilium where it regulated ciliary composition and signalling [28, 29]. However, cilium-associated functions for DLG1 have so far not been reported.

The physiological importance of DLG1 in vertebrates is highlighted by the fact that *Dlg1* gene-trap mutant mice display neonatal lethality, growth retardation, craniofacial abnormalities, and small kidneys characterized by impaired ureteric bud branching and reduced nephron formation [30, 31]. Similarly, complete knock out of *Dlg1* in the mouse was shown to cause neonatal lethality due to severe defects in e.g. cardiovascular and craniofacial development as well as defective formation of urogenital organs [32, 33]. With respect to the latter, *Dlg1* knockout animals appeared to lack the stromal cells that normally lie between the urothelial and smooth muscle layers, and the circular smooth muscle cells in the ureteric smooth muscle were misaligned, giving rise to impaired ureteric peristalsis and hydronephrosis [32]. Conditional ablation of *Dlg1* in the metanephric mesenchyme, which gives rise to the various segments of the mature nephron, resulted in formation of glomerular cysts, dilated proximal tubules, protein casts, and diffuse areas of inflammation. The kidneys appeared grossly cystic in contrast to controls, and the mice showed elevated levels of blood urea nitrogen and serum creatinine, indicative of renal failure [34].

In humans, *DLG1* was identified as a susceptibility gene for congenital anomalies of the kidney and urinary tract (CAKUT) [35], and a missense variant in DLG1 (p.T489R) was indeed identified in a patient with CAKUT [36]. Furthermore, *DLG1* is deleted in the 3q29

120 microdeletion syndrome that is characterized by mild-to-moderate mental retardation, a long
121 and narrow face, as well as additional phenotypes such as microcephaly, cleft lip and palate,
122 horseshoe kidney and hypospadia [37]. However, while emerging evidence suggests that
123 mutations in ciliary genes can give rise to CAKUT [38], it is unclear whether some of the
124 kidney phenotypes observed in mice and patients with *DLG1* mutations, are linked to ciliary
125 defects.

126 Here we investigated a potential role for DLG1 in ciliary biogenesis and function by
127 using a previously described kidney specific conditional *Dlg1* mouse knockout model [39], as
128 well as cultured kidney epithelial cells. Loss of *Dlg1* in mouse kidney led to ciliary
129 elongation and cortical cyst formation whereas cell-based proximity labelling proteomics and
130 fluorescence microscopy implicated DLG1 in regulating the ciliary protein composition.
131 Specifically, cilia from cells lacking DLG1 contained less SDCCAG3, IFT20 and PC2 than
132 control cells, and re-expression of wildtype DLG1, but not a CAKUT-associated DLG1
133 missense variant, could rescue this phenotype. Despite its role in regulating ciliary length and
134 composition in kidney epithelial cells, DLG1 was primarily localized to the lateral plasma
135 membrane in these cells. Finally, in agreement with its role in promoting ciliary localization
136 of SDCCAG3 and IFT20, immunoprecipitation assays indicated that DLG1, SDCCAG3 and
137 IFT20 interact with each other, and Alpha Fold modelling furthermore suggested that
138 SDCCAG3 and IFT20 may bind directly to each other. Our work thus identifies a key role for
139 DLG1, located at the lateral plasma membrane of kidney epithelial cells, in mediating ciliary
140 targeting of PC2 and other proteins and supports emerging evidence linking ciliary
141 dysfunction to CAKUT.

142

143

Results

Kidney-specific ablation of *Dlg1* in mouse causes ciliary elongation. To investigate possible ciliary functions for DLG1, we analyzed kidneys from *Pax3Cre-Dlg1*$^{F/F}$ mice in which *Dlg1* is conditionally knocked out in the majority of kidney cells. Of note, *Pax3Cre* is expressed in the metanephric mesenchyme that differentiates to form the various segments of the mature nephron (glomerulus, proximal tubule, loop of Henle, and distal tubule). Therefore, *Pax3Cre-Dlg1*$^{F/F}$ mice result in loss of *Dlg1* expression in all nephron (but not ureteric bud) epithelial cell derivatives. These mice display a congenital hydronephrosis phenotype (Figure 1A) similar to that observed in the global *Dlg1*$^{-/-}$ mutant mice [32], as well as tubular dilations that appeared to be pre-cystic (Figure 1A) [39]. The cystic dilations are consistent with prior experiments, where ablation of *Dlg1* in the metanephric mesenchyme (using Six2-Cre) also resulted in the formation of tubular cysts in the kidney cortex [34]. The *Pax3Cre* transgene is also active in urogenital mesenchyme, and it was concluded that the lack of DLG1 in these cells results in the observed structural and functional defects in the ureter that cause hydronephrosis [39]. Loss of DLG1 resulted in a significant increase in cilia length and acetylated tubulin staining intensity in pre-cystic nephron tubules (Figure 1B-D), indicating that DLG1 plays an essential role in regulating ciliary biogenesis and/or maintenance during kidney development *in vivo*. Supportively, knock out of *Dlg1* in mouse kidney cortical collecting duct (mCCD) cells [40] did not affect ciliation frequency but led to significant ciliary lengthening when cells were grown on transwell filters, which ensures full cell polarization, a phenotype that was rescued by stable re-expression of mCherry-DLG1 (Figure 1E-H). In contrast, under standard culture conditions the *Dlg1*$^{-/-}$ mCCD cells displayed cilia of normal length (Figure S1A), indicating that the ciliary length phenotype manifests itself only when cells are fully polarized. Quantitative RT-PCR analysis showed that in addition to *Dlg1*, mCCD cells also express *Dlg4* and a small amount of *Dlg3*, but the

relative expression levels of these mRNAs and of *Dlg2* were not altered in the *Dlg1*$^{-/-}$ cells relative to wild type (WT) cells (Figure S1B, C). Thus, the ciliary length phenotype observed in the *Dlg1*$^{-/-}$ cells is not caused by altered expression of *Dlg2, 3 or 4*.

DLG1 localizes to the lateral plasma membrane in polarized kidney epithelial cells. To address how DLG1 might regulate ciliary length we investigated its subcellular localization in transwell filter-grown mCCD cells by immunofluorescence microscopy (IFM) analysis. Under these conditions endogenous DLG1 localized to the lateral membrane as expected and was not detected at the cilium-centrosome axis (Figure S1D). We similarly investigated the subcellular localization of endogenous and tagged versions of DLG1 in IMCD3 cells, but despite intense efforts we only observed DLG1 localization at the plasma membrane and not the primary cilium of these cells (data not shown). Since previous proteomics analyses detected DLG1 in cilia of IMCD3 cells and mouse photoreceptor outer segments following actin depolymerization or loss of Bardet-Biedl syndrome proteins [24-26], we surmise that DLG1 may localize to cilia under certain conditions and/or is undetectable in cilia by IFM of mCCD and IMCD3 cells for technical reasons. Supportively, eGFP-DLG1 transiently overexpressed in retinal pigment epithelial (RPE1) cells was highly concentrated at the base of and within the cilium (Figure S1E), indicating that DLG localizes to the cilium-centrosome axis under some conditions. Nevertheless, taken together our results suggest that DLG1 regulates ciliary length in polarized kidney epithelial cells indirectly, i.e. at the level of the lateral plasma membrane.

Loss of DLG1 causes altered ciliary protein content in IMCD3 cells. Ciliary length control is complex and regulated by a variety of factors and signalling pathways that modulate the polymerization/depolymerization of the ciliary axoneme or affect ciliary membrane dynamics; changes in ciliary protein composition that affect signalling output can therefore also affect ciliary length [41, 42]. As an example, kidney epithelial cell cilia from

patients with ADPKD or from *Pkd1* and *Pkd2* knockout mice were shown to be elongated, possibly due to altered signalling [43, 44]. To investigate how DLG1 might affect ciliary protein composition, we used an unbiased cilium-targeted proximity labelling approach [24] by taking advantage of previously described IMCD3 cell lines stably expressing a ciliary NPHP3[residues 1-203]-BioID2 fusion protein (hereafter called cilia-BioID2) or BioID2 alone (hereafter called BioID2) [45]. We then knocked out *Dlg1* in these lines with the aim of determining how loss of DLG1 affects the ciliary proteome. Western blot analysis confirmed the loss of DLG1 in both the cilia-BioID2 and BioID2 *Dlg1*$^{-/-}$ lines (Figure S2A). Meanwhile, IFM analysis of serum-starved cells incubated with biotin and stained with an antibody against acetylated α-tubulin (ciliary axoneme marker), and green-fluorescent streptavidin showed prominent ciliary enrichment of biotinylated proteins in both cilia-BioID2 lines, whereas biotinylated proteins were confined to the cell body of the BioID2 lines, as expected (Figure S2B). Under these conditions we did not observe any differences between WT and *Dlg1*$^{-/-}$ lines with respect to ciliary length (Figure S2C) and ciliation frequency (Figure S2D), as observed in standard cultures of mCCD cells (Figure S1A). Finally, by quantitative RT-PCR we found that IMCD3 cells express similar amounts of *Dlg1* and *Dlg4* (Figure S2E, F) and knockout of *Dlg1* did not cause altered expression of *Dlg2, 3 or 4* in these cells (Figure S2G, H).

Having validated our WT and *Dlg1*$^{-/-}$ cilia-BioID2 and BioID2 lines, we next analyzed the ciliary proteome of these cells by subjecting them to biotin labeling followed by streptavidin pull-down and mass spectrometry. Mass spectrometry analysis resulted in the identification of a total of 2100 proteins across 6 experimental replicates per cell line. Our analysis focused solely on proteins that are potentially altered in the primary cilium; therefore, we disregarded the proteins that were significantly altered in the BioID2 control condition. These were further subdivided into three Tiers based on stringency criteria. Tier 1

(q-value ≤0.05 and Sign. A ≤ 0.05) comprised 118 highly significantly altered proteins, from which 84 proteins were depleted from the cilium, whereas 34 proteins were enriched (Figure 2A). The rest of the proteins were divided into Tier 2 (Sign. A ≤0.05), Tier 3 (q-value ≤0.05), and non-significant (NS) when a less stringent cut-off was applied (Figure 2A, Supplementary Table S1). Using the Tier 1 proteins identified in our dataset, a comprehensive GO term enrichment analysis was performed to pinpoint the functional roles of the proteins regarding DLG1's impact on cilium composition. This analysis focused on the two GO categories: Biological Process (BP) and Cellular Component (CC) (Figure 2B, C). The BP terms were, in turn, analyzed separately for the depleted and enriched proteins within the cilium (Figure 2B). For the depleted proteins, the significant BP terms were pertaining to intraciliary transport, cilia assembly and organization as well several signalling pathways. Moreover, in the GO-CC term category, 15 terms were significant, out of which seven terms were associated with ciliary components (Figure 2C). On the other hand, for the enriched proteins, BP terms related to the regulation of cell cycle transitions and mitochondrial gene expression were highly significant (Figure 2B). Altogether, the proximity labeling approach yielded a dataset indicating a role for DLG1 in regulating ciliary composition in IMCD3 cells.

DLG1 is required for ciliary targeting of SDCCAG3 and IFT20 in kidney epithelial cells. To validate the results of our proximity labelling proteomics analysis, we initially focused on the Tier 1 candidates SDCCAG3 and IFT20, which both appeared to be significantly depleted from cilia of *Dlg1*$^{-/-}$ cells compared to WT (Figure 2A; Supplementary Table S1). SDCCAG3 is known to bind to the core retromer subunit VPS35 [46], and was shown to localize to the base of primary cilia in cultured mammalian cells, including IMCD3 cells, where it also promoted ciliary targeting of PC2 [15]. Similarly, IFT20 has a well-established role in conferring targeting of PC2 from the Golgi to the primary cilium [7, 13,

14] and is also part of the IFT-B complex involved in IFT within cilia [47]. Analysis of ciliated *Dlg1*$^{-/-}$ and WT cilia-BioID2 IMCD3 cells by IFM with antibodies specific for SDCCAG3 confirmed that its ciliary localization is significantly reduced in the *Dlg1*$^{-/-}$ cells compared to WT (Figure 3A, B), whereas total cellular levels were unchanged (Figure 3C). Stable expression of mCherry-DLG1 in the *Dlg1*$^{-/-}$ cilia-BioID2 IMCD3 cells could restore ciliary levels of SDCCAG3 to normal (Figure 3A, B, D), and similar results were obtained in mCCD cells (Figure 3E-G; see also Figure 5E, F). Using similar approaches, we confirmed that loss of DLG1 causes reduced ciliary base levels of IFT20 in mCCD cells; in the cilia-BioID2 IMCD3 cells, DLG1 loss had a similar effect although the reduction in IFT20 cilia base staining intensity was not statistically significant compared to WT cells (Figure S3A-D). The reason for this cell-type specificity is unclear but may be due to relatively high background staining of IFT20 in the cilia-BioID2 IMCD3 under the specific fixation conditions used. Notably, IFM analysis of kidney sections from WT and *Pax3Cre-Dlg1*$^{F/F}$ mice showed that ciliary levels of SDCCAG3 and IFT20 are significantly reduced in the *Dlg1* knockout compared to control (Figure 4), indicating that DLG1 promotes ciliary targeting of SDCCAG3 as well as IFT20 *in vivo*. Since DLG1 was previously shown to interact physically and functionally with exocyst complex component SEC8 [48, 49], which in turn mediates ciliary membrane biogenesis and PC2 trafficking [7, 50, 51], we also analyzed whether loss of DLG1 affected ciliary presence of SEC8 in cilia-BioID2 IMCD3 or mCCD cells. However, while this analysis confirmed that SEC8 is concentrated at the ciliary base, we did not observe any significant change in ciliary base levels of SEC8 in *Dlg1*$^{-/-}$ cells compared to WT cells (Figure S4). We conclude that DLG1 is required for localizing SDCCAG3 and IFT20, but not SEC8, to the primary cilium of kidney epithelial cells *in vitro* and *in vivo*.

Loss of or acute inhibition or DLG1 impairs ciliary targeting of PC2. Given the known roles of SDCCAG3 and IFT20 in promoting vesicular trafficking of PC2 to the primary cilium [13-15], we asked if DLG1 regulates ciliary PC2 trafficking. Although PC2 was not detected in our cilia-BioID2 proximity labelling dataset from IMCD3 cells (Figure 2A; Supplementary Table S1), we reasoned this could be due to technical reasons or the cell line used. We therefore used mCCD cells to directly test if inhibition or depletion of DLG1 affected ciliary PC2 levels. First, we cultivated our WT, *Dlg1*$^{-/-}$ and rescue mCCD lines on transwell filters to ensure full polarization of the cells. Confocal 3D imaging showed that the cells were indeed fully polarized under these conditions, and no apparent polarity defects were observed in the *Dlg1*$^{-/-}$ cells compared to the WT and rescue line (Figure 5A, B). Moreover, the transwell filter-grown *Dlg1*$^{-/-}$ cells also displayed significantly reduced ciliary levels of PC2 compared to the WT cells and this phenotype was rescued by stable expression of mCherry-DLG1 (Figure 5C, D). For robust and unbiased quantification of ciliary PC2 levels, we employed a MATLAB-based approach (see Material and Methods for details) for automatic and high throughput quantitative analysis of ciliary fluorescent staining intensity in transwell filter-grown mCCD cells. Using this approach, we were also able to confirm our results obtained for SDCCAG3 in mCCD cells grown under standard culture conditions, namely a significantly reduced ciliary presence of SDCCAG3 in *Dlg1*$^{-/-}$ cells compared to WT and rescue lines (Figure 5E, F).

To confirm that DLG1 regulates ciliary PC2 trafficking, we took advantage of two previously described peptide inhibitors, AVLX-144 (Tat-N-Dimer) and ReTat-N-dimer [52] to specifically block the first and second PDZ domain of DLG1 in ciliated WT mCCD cells. We subsequently analyzed the cells by IFM and staining for PC2 in the treated cells; the cilium was visualized by staining with acetylated α-tubulin antibody. We found that treatment of mCCD ciliated cells with both AVLX-144 and ReTat-N-Dimer caused a significant depletion

of PC2 from the ciliary base and along the cilium. Importantly, incubation with the control peptide AVLX-144-AA, which is a structurally similar to AVLX-144 and ReTAT-N-dimer, but non-binding to PDZ domains [53], did not affect PC2 ciliary levels (Figure S5). This result indicates that DLG1 is indeed required for targeting of PC2 to the primary cilium, and that the impaired ciliary targeting of PC2 to the cilium observed upon DLG1 inhibition is not secondary to cytokinesis [54, 55] or polarity defects [18].

We conclude that DLG1 is required for targeting PC2 to the primary cilium of kidney epithelial cells, and that the alterations in ciliary composition observed in *Dlg1*$^{-/-}$ cells are not due to cytokinesis or polarity defects. Furthermore, we conclude that DLG1-mediated ciliary targeting of PC2 requires DLG1's first two PDZ domains.

A CAKUT-associated DLG1$^{T507R/T489R}$ missense variant fails to rescue the ciliary phenotype of *Dlg1*$^{-/-}$ cells. A previous study identified a DLG1 missense mutation (p.T489R; hereafter referred to as DLG1^{T489R}) in a patient with CAKUT (Table S4 in [36]). To investigate a possible ciliary involvement in this disorder, we tested if exogenous expression of the rat equivalent of the human DLG1^{T489R} missense variant, DLG1^{T507R} (Figure 6A), could rescue the ciliary phenotype of *Dlg1*$^{-/-}$ cells. To this end, we generated a lentiviral construct that we used for stable expression of mCherry-DLG1^{T507R} in the *Dlg1*$^{-/-}$ mCCD cells (Figure 6B). Interestingly, when cells were grown on transwell filters, the DLG1^{T507R} variant failed to rescue the ciliary elongation phenotype observed in the *Dlg1*$^{-/-}$ cells (Figure 6C). Furthermore, while stable expression of mCherry-tagged WT DLG1 fully restored ciliary base levels of IFT20 (Figure S3C, D) and SDCCAG3 (Figure 3E, F) in mCCD cells, this was not the case for the DLG1^{T507R} variant (Figure 6D-G). This suggests that ciliary defects may contribute to the CAKUT disease aetiology of patients harbouring the DLG1^{T489R} mutation although we cannot rule out that this mutation separately affects cilia and causes CAKUT.

We also tested the impact of the DLG1^{T507R} variant on the ciliary levels of PC2 by IFM analysis of transwell filter-grown mCCD cells. Our findings indicated that the DLG1^{T507R} variant can partially restore the ciliary levels of PC2 to normal in the *Dlg1*$^{-/-}$ background although not to the same extent as WT DLG1 (Figure S6). This suggests that this specific point mutation in DLG1 has a more severe impact on ciliary targeting of SDCCAG3 and IFT20 than PC2, implying that DLG1 promotes ciliary PC2 trafficking not only via SDCCAG3 and IFT20.

Loss of DLG1 leads to constitutive phosphorylation of TAK1. Upon analysing the GO-BP terms of our proteomics data (Figure 2B) we noticed that several proteins responsible for regulating MAP kinase activity, such as mitogen-activated protein kinase kinase kinase 7 (MAP3K7, hereafter referred to as Transforming growth factor beta (TGFβ) Activated Kinase 1, TAK1), are diminished in the primary cilium of *Dlg1*$^{-/-}$ cells. As TAK1 is linked to the pathogenesis of kidney fibrosis stimulated by TGFβ ligands [56, 57] and since TGFβ signalling is orchestrated by the primary cilium [58, 59] we investigated the potential impact of *Dlg1* loss on TGFβ signalling. Upon stimulation with TGFβ-1 ligand, we observed that activation of SMAD2 as evaluated by its phosphorylation on Ser465/467 in the canonical branch of TGFβ signalling was largely unaffected in ciliated *Dlg1*$^{-/-}$ as compared to WT mCCD cells (Figure 6H, I). In contrast, we observed that phosphorylation of TAK1 on Thr184/187 and S412 marking full activation of this MAP kinase was increased in unstimulated *Dlg1*$^{-/-}$ cells as compared to WT cells (Figure 6J, K). These results indicate that DLG1 takes part in the regulation of sub-pathways in TGFβ signalling, although further studies are needed to delineate the mechanisms by which DLG1 restricts basal levels of TAK1 activation, and whether such mechanisms are controlled at the level of primary cilia.

DLG1 associates physically with SDCCAG3 and IFT20. Finally, to address the mechanism by which DLG1 promotes targeting of SDCCAG3 and IFT20 to the primary

cilium, we tested if DLG1 interacts with these proteins. Indeed, immunoprecipitation (IP) of lysates from HEK293T cells co-expressing GFP-DLG1 and SDCCAG3 or IFT20 fusion proteins indicated that DLG1 interacts with both SDCCAG3 and IFT20 (Figure 7A, B). Similarly, IP analysis in HEK293T cells demonstrated interaction between SDCCAG3 and IFT20 (Figure 7A). To determine the molecular basis for these interactions we used Alpha Fold modelling [60] and identified a high confidence interaction between SDCCAG3 and IFT20 (Figure 7C; Figure S7) but did not obtain strong evidence indicative of direct binding of these two proteins to DLG1. Moreover, the predicted interaction between IFT20 and SDCCAG3 is mutually exclusive with binding of IFT20 to its known partner within the IFT-B complex, IFT54 [61] (Figure 7C). IFT20 was shown previously to interact with the BLOC-1 complex [7], and the BLOC-1 complex subunit DTNBP1 (dysbindin) binds directly to DTNA and DTNB (α- and β-dystrobrevin, respectively) of the dystrophin-glycoprotein complex (DGC) [62]. Interestingly, we and others have previously shown that DLG1 as well as its direct interactor, KIF13B, bind to components of the DGC, including UTRN, DTNA and DTNB [63, 64]. Furthermore, a high throughput study indicated that SDCCAG3 also binds DTNBP1 [65]. Therefore, we hypothesize that DLG1 may associate with IFT20 and SDCCAG3 through DTNBP1-DTNA/B interactions but more work is needed to clarify this. In summary, the IP and Alpha Fold modelling results suggest that SDCCAG3 and IFT20 form a hetero-dimeric complex that associates, at least indirectly, with DLG1.

Discussion

Here we demonstrated that DLG1 is important for regulating the length and composition of primary cilia in kidney epithelial cells, both in cultured cells and *in vivo*. Using an unbiased cilium-targeted proteomics approach, we show that loss of DLG1 in IMCD3 cells causes altered ciliary protein content with most of the affected proteins being diminished in the

cilium of *Dlg1*$^{-/-}$ cells. Specifically, loss DLG1 led to reduced ciliary levels of SDCCAG3 and IFT20, which have both been shown to confer ciliary targeting of PC2 [13-15]. Consistently, we also established a requirement for DLG1 in promoting ciliary targeting of PC2 in mCCD cells, although our results with a CAKUT-associated missense variant indicated that DLG1 not only confers ciliary targeting of PC2 via SDCCAG3 and IFT20. Reduced ciliary presence of polycystins may at least be partly responsible for the observed ciliary length phenotype of DLG1-deficient cells as loss of PC1 or PC2 was shown to induce ciliary lengthening in kidney epithelial cells [43, 44], but alternative mechanisms cannot be ruled out. From a human disease perspective PC2 is highly relevant as mutations in its corresponding gene (*PKD2*) cause ADPKD [66], and appropriate ciliary localization of PC2 is critical for its function [9]. SDCCAG3 and IFT20 seem to promote ciliary trafficking of PC2 primarily at the level of the recycling endosome and cis-Golgi [7, 13-15], and exocyst complex components also impact the ciliary targeting of PC2 [7]. The exocyst complex tethers vesicles at target sites before membrane fusion [67], and DLG1 binds exocyst complex component SEC8 [48, 49]. However, loss of DLG1 did not affect the ciliary base localization of SEC8 in IMCD3 or mCCD cells.

Although DLG1 may localize to primary cilia under some conditions [24-26], our results indicated that in polarized kidney epithelial cells DLG1 is largely confined to the lateral plasma membrane in agreement with its well-known role as a core component of the Scribble polarity complex. The Scribble complex, which consists of DLG1, Scribble (SCRIB) and lethal giant larvae (LGL), plays a central role in orchestrating epithelial cell polarity [68], and Scribble complex components were also implicated in protein cargo sorting and vesicle transport. For example, a study in mouse hippocampal neurons found that DLG1 regulates clathrin-mediated endocytosis of AMPA receptors by recruiting myosin VI and AP-2 adaptor complex to endocytotic vesicles containing these receptors [69]. Furthermore, in *Drosophila*

the Scribble complex is required for proper localization of retromer components to endosomes and promotes appropriate sorting of cargo in the retromer pathway [70], consistent with our finding that DLG1 associates with and regulates ciliary localization of retromer-associated protein SDCCAG3. Studies have demonstrated that deficiency of retromer regulator sorting nexin-17 (SNX17) and SDCCAG3 disrupt ciliogenesis [15, 71]. Moreover, the retromer complex interacts with the N-terminal cytoplasmic domain of PC2, and the disruption of this interaction impairs the ciliary localization of PC1 [16]. Since DLG1 localizes predominantly to the lateral plasma membrane in polarized kidney epithelial cells our results are consistent with a model whereby DLG1 regulates internalization of ciliary cargoes (SDCCAG3, IFT20, PC2) that are transiently transported to this site prior to their onward journey via recycling endosomes to the primary cilium (Figure 7D). Notably, the Na^+,HCO_3^- cotransporter NBCn1 (SLC4A7), which localizes at the lateral membrane and primary cilium of polarized kidney epithelial cells, interacts tightly with DLG1 [72], and multiple retromer components were identified as putative NBCn1 binding partners in GST pulldown assays [73]. Furthermore, our proteomics analysis identified the Na^+/H^+ exchanger NHE1 (SLC9A1) and the cation channel TRPV4 as Tier 1 candidates depleted from cilia in the *Dlg1*$^{-/-}$ cells (Figure 2; Table S1). This suggests that DLG1 and the retromer complex may regulate ciliary trafficking of a range of ion channels and transporters, in addition to PC2. Future research should be aimed at addressing this possibility.

Epithelial cells rely on highly organized trafficking machinery to maintain their polarity and carry out their epithelial functions. Such trafficking involves several factors, including sorting signals, cytoskeletal network, vesicle tethering complexes, and Rab and Rho GTPases, that determine the final destinations of each protein [74]. Importantly, the cellular microtubule cytoskeleton of polarized epithelial cells is organized very differently compared to mesenchymal cells, with microtubules aligning parallel to the apico-basal axis

and extending their plus ends towards the basal surface [75] (Figure 7D). Therefore, post-Golgi vesicle trafficking in epithelial cells often occurs via indirect transport routes, such as transcytotic or recycling endosomal routes, to ensure delivery of membrane cargo to the apical surface or ciliary compartment [7, 9, 75]. In addition to the lateral plasma membrane functioning as a docking site for ciliary components, prior to their final transport to the cilium, the apical membrane domain may also function as a transit point for ciliary protein trafficking. For example, nephronophthisis proteins NPHP1, NPHP4, and NPHP8 not only localize to the transition zone, but also accumulate at cell junctions, e.g. in polarized kidney epithelial cells [76], where they interact with Crumbs polarity complex components (PATJ, PALS1, PAR6) [77], which are concentrated at the apical-lateral border, just above the tight junctions [78]. Conversely, accumulating evidence suggests that components of the Crumbs complex localize to cilia and regulate ciliary assembly or function [64, 79, 80]. Notably, our proteomics analysis identified PATJ (INADL) as a Tier 1 candidate depleted from cilia in the *Dlg1*$^{-/-}$ cells (Figure 2; Table S1) and PC2 was also shown to bind to the Crumbs complex component PALS1 [81], suggesting that multiple polarity complexes located along the apical-basal border of epithelial cells may function together to regulate ciliary protein cargo transport. More studies will be needed to explore this in more detail and define the precise mechanisms involved.

Our cilia proteomics analysis identified several proteins that affect energy homeostasis and NFκB and TGFβ signalling, and which were depleted from cilia of *Dlg1*$^{-/-}$ cells. These include TAK1, whose kinase activity is critical for regulating a variety of cell functions relevant for kidney development and function [82]. Interestingly, our cell-based assays showed that disruption of DLG1 leads to over-activation of TAK1 in line with a recent study, showing that *Dlg1* deficiency in mouse microglial cells impairs microglial activation and prevents production of inflammatory cytokines [83]. Furthermore, multiple lines of

443 evidence have shown that alterations in ciliary length and inactivation of polycystins can
444 cause profound metabolic rewiring in the kidney, which likely contributes to development of
445 PKD [84-86]. Nevertheless, if and how altered ciliary length and composition, as well as
446 dysregulated metabolic, NFκB and TGFβ signalling, contribute to the kidney defects
447 observed in *Dlg1* deficient mice and human CAKUT patients with *DLG1* mutations awaits
448 further investigation. However, we note that a more distantly related DLG1 homolog, DLG5,
449 has been implicated in ciliary biogenesis and function as well as in CAKUT [87, 88],
450 supporting the involvement of cilia and DLG proteins in this disease.

451

452 Materials and methods

453 **Mammalian cell culture.** IMCD3 cells stably expressing NPHP3[residues 1-203]-BioID2
454 (hereafter called cilia-BioID2) and BioID2 alone (hereafter called BioID2) have been
455 described previously [45]. IMCD3 cells were cultured in DMEM/F-12, GlutaMAX
456 Supplement (Gibco, cat. #31331-093) medium supplemented with 10% fetal bovine serum
457 (FBS; Gibco, cat. #10438-026) and 1% Penicillin-Streptomycin (Sigma-Aldrich, cat.
458 #P0781). The immortalized mCCD parental/WT cell line was generously provided by Dr.
459 Eric Féraille (University of Lausanne, Switzerland) and has been described previously [40]
460 The mCCD cells were cultured as described in [40], and RPE1 cells stably expressing SMO-
461 tRFP [89] were cultured and transfected as described in [29]. Human embryonic kidney
462 (HEK) 293T cells were from ATCC (cat. #CRL-3216) and were cultured in high-glucose
463 DMEM (Gibco, cat. #41966-052) supplemented with 10% FBS and 1% Penicillin-
464 Streptomycin.

465 All cell lines were grown in a 95% humidified incubator at 37 °C with 5% CO_2. To
466 induce ciliogenesis, IMCD3 cells were grown in plain DMEM/F-12, GlutaMAX Supplement

for 24 h, while mCCD cells were grown in starvation medium, where the serum and hormone-deprived DMEM/F12, GlutaMAX Supplement medium was supplemented with 5 µg/ml holo-transferrin (Sigma-Aldrich, cat. # T0665) and 60 nM sodium selenite (Sigma-Aldrich, cat. #S5261) for 24 h.

Transwell culture system. For setting up fully polarized epithelial cells, mCCD cells were grown in full DMEM/F-12, Glutamax Supplement medium as described above, using Thermo Scientific™ Nunc™ Polycarbonate Membrane Inserts in Multidishes (Thermo Scientific, cat. #140652), which have a pore size of 0.4 µm. This was done for a duration of 10 days before proceeding with further experiments. The medium was replaced every 3 to 4 days. For IFM analysis, the polarized mCCD cells were fixed and membrane inserts were excised and treated as described in the general IFM protocol (see below).

Generation of *Dlg1*$^{-/-}$ cell lines. To knock out *Dlg1* in the kidney epithelial cell lines, we employed CRISPR/Cas9 technology and used four sgRNA sequences from the mouse CRISPR "Brie" Knockout Library [90]. The sequences are provided in Table 1. The sgRNA spacers were cloned into pSpCas9(BB)-2A-Puro (PX459) V2.0 plasmid (Addgene, cat. #62988) as described previously [91]. This involved phosphorylating and annealing the two complementary sgRNA oligos, which were then ligated into the BbsI-digested backbone. Then the selected clones were sequenced to verify the spacer sequence. The parental (WT) cilia-BioID2 and BioID2 IMCD3 lines, and the WT mCCD cells were transfected with the Cas9-gRNA plasmids (pool of all four gRNAs) using reverse transfection with Lipofectamine 3000 Transfection Reagent (Invitrogen, cat. #L3000015) according to the manufacturer's instructions. A day after transfection, cells were treated with 2 µg/ml puromycin (Invitrogen, cat. #A11138-03) for 72 h and then tested for DLG1 protein depletion by western blot analysis. Subsequently, the cells underwent single cell sorting at the FACS Facility at Biotech Research & Innovation Centre (University of Copenhagen, Copenhagen, DK). The selected

clones were validated by western blot analysis and Sanger sequencing to confirm the occurrence of the indel event.

Generation of transgenic cell lines. A plasmid containing the full-length rat *Dlg1* coding sequence [92] was used as template for cloning the rat *Dlg1* coding sequence into Gateway entry plasmid pENTR220-mCherry-C1 using standard cloning techniques. This entry plasmid was then recombined with pCDH-EF1a-Gateway-IRES-BLAST destination plasmid through LR reaction using the Gateway LR Clonase II Enzyme mix (Invitrogen, cat. #11791020). The cloning vectors used were generously provided by Dr. Kay Oliver Schink (Oslo University Hospital, Norway), and were described in [93]. The lentiviral expression plasmids were later subjected to site-directed mutagenesis, performed by GenScript, to create a double-point mutation on the following sites: c.1520C>G and c.1521T>A; p.T507R. Lentiviral particles were generated by co-transfecting the lentiviral expression plasmids with second-generation lentiviral packaging vectors pMD2.G and pCMVΔ-R8.2 into HEK293T cells (kindly provided by Dr. Carlo Rivolta, Institute of Molecular and Clinical Ophthalmology Basel, Switzerland) using Lipofectamine 3000 Transfection Reagent (Invitrogen, cat. #L3000015) according to the manufacturer's instructions. The harvested culture medium containing lentiviral particles coding for either WT DLG1 or DLG1^{T507R} fusion proteins were used to transduce the kidney epithelial cells. Cells were selected using 5-15 µg/ml Blasticidin S (Gibco, cat. #R21001) and expression was confirmed with western blotting and live cell fluorescence microscopy.

BioID2 proximity labeling. We conducted a proximity labeling experiments, which involved the WT and *Dlg1*$^{-/-}$ cilia-BioID2 lines described above, with the WT and *Dlg1*$^{-/-}$ BioID2 lines as negative controls. The cells were plated in 15 cm dishes and cultured in normal medium containing DMEM/F-12, GlutaMAX Supplement (Gibco, cat. #31331-093) supplemented as described above. Once the cells had reached 80% confluency, they were stimulated for

ciliogenesis for 24 h with the medium described above. Proximity labeling was induced overnight by supplementing the medium with 10 μM Biotin (Sigma-Aldrich, cat. #B4501). The cells were lysed, and samples were prepared for mass spectroscopy according to a previously published BioID2-based proximity labeling protocol [45].

Mass spectroscopy and data analysis. The samples were analyzed and proteins were identified according to the method described in [45]. For proteomics data analysis, we used a custom in-house R script that replicates the analysis using the Perseus software [94]. The LFQ intensity values were compared for cilia-BioID2 WT samples versus those for cilia-BioID2 *Dlg1*$^{-/-}$ samples and for BioID2 WT samples versus BioID2 *Dlg1*$^{-/-}$ samples. For samples where LFQ intensity values were zero in less than half of the replicates, while having non-zero LFQ intensity values in the other replicates, imputed values were applied drawn from a normal distribution that had a mean that was 1.8 times below the mean of the non-zero values and a standard deviation that was 0.5 times the mean. Subsequently, Student's t-test was used for statistical comparisons between the LFQ intensity values of samples as well as the significance A test to infer samples with outlier log2 ratios (high or low). After removing the proteins that were significantly altered in the BioID2 comparison, we devised a three-tier system to classify significant proteins from the cilia-BioID2 comparison. Tier 1 proteins were ones where the corrected p-values (Benjamini-Hochberg correction) from the t-test were < 0.05 as well as significance A test p-values were < 0.05. Tier 2 proteins included proteins that only had significance A test p-values < 0.05 and Tier 3 proteins were the ones that only had corrected p-values from the t-test < 0.05.

GO term enrichment analysis. To conduct the analysis, the topGO package [95] in R was utilized on the Tier 1 proteins, comprising 118 proteins in total. The approach involved using the GO terms (Biological Process – BP and Cellular Component – CC) linked with all the proteins in the proteomics data analysis and carried out an enrichment analysis for each GO

category using Fisher's exact test. Next, a maximum of the top 30 terms were sorted by the Odds ratio and with Fisher's test corrected p-value < 0.05 and removed the redundancy in the enriched terms to leave only the terms that were specific and perhaps more informative. This was achieved by removing the other terms that were ancestral in the same GO lineage as the term of interest.

Immunofluorescence microscopy analysis and live cell imaging. IMCD3 and mCCD cells were trypsinized (2x concentration, Sigma Aldrich, cat. #T4174), seeded, and grown on 12-mm diameter glass coverslips. Upon reaching 80% confluence, cells were starved for 24 h to induce robust ciliogenesis using the aforementioned media. The coverslips were fixed in 4% paraformaldehyde (PFA; Sigma, cat. #47608) in PBS for 12 min either at room temperature or at 4 °C, washed with PBS, and incubated in permeabilization buffer (0.2% Triton X-100, 1% BSA in PBS) for 12 min before blocking and antibody incubation. The fixed cells were blocked in 2% (w/v) BSA-based blocking buffer, then incubated with primary antibodies diluted in 2% BSA for 1.5-2 h at room temperature or overnight at 4 °C. After extensive washing with PBS, cells were then incubated with secondary antibodies diluted in 2% BSA in PBS for 1 h at room temperature. Last, nuclei were labeled with DAPI (Sigma-Aldrich, cat. #D9542). Antibodies and dilutions used in this study for IFM are listed in Table 1. For IFT20 staining, we followed an IFM protocol method described in [96] where we briefly washed the cells with cytoskeletal buffer, then immediately fixed them with ice-cold MeOH inside a -20 °C freezer. For PC2 and SEC8 staining, we used an IFM protocol method described in [97]. All coverslips were mounted with 6% propyl gallate (Sigma-Aldrich, cat. #P3130) diluted in UltraPure Glycerol (Invitrogen, cat. #15514-001) and 10xPBS and combined with Epredia Immu-Mount (Epredia, cat. #9990402) in a 1:12 ratio.

Images of cells seeded on coverslips were obtained with an Olympus BX63 upright microscope equipped with a DP72 color, 12.8 megapixels, 4140x3096 resolution camera, and

Olympus UPlanSApo 60x oil microscope objective. Images of the transwell filter-grown polarized epithelial cells were obtained with an Olympus IX83 inverted microscope, equipped with a Yokogawa CSU-W1 confocal scanner unit, ORCA-Flash4.0 V3 Digital CMOS camera (type number: C13440-20CU), and Olympus UPlanSApo 100x oil microscope objective. To prepare the images for publication, we used cellSens 1.18 software for constrained iterative deconvolution and assembled montages with Fiji and Adobe Photoshop 2023.

Live cell imaging of RPE1 cells stably expressing SMO-tRFP and transiently expressing eGFP-DLG1 was done as described in [29].

Immunofluorescence staining of kidney sections. The mouse kidney specimens assayed for ciliary length, SDCCAG3 and IFT20 localization were obtained from *Pax3Cre-Dlg1*$^{F/F}$ mice and control (WT) littermates that were previously described [39]. For immunofluorescence staining of paraffin-embedded sections, antigen unmasking was performed by boiling the slides in antigen-retrieval buffer (10 mM Tris Base, 1 mM EDTA, and 0.05% Tween-20, pH 9.0) for 30 min. Samples were permeabilized with 0.05% Triton X-100 in PBS (PBS-T) for 10 min at room temperature, incubated in blocking buffer (3.0% BSA and 0.1% Triton X-100 in PBS) for 1 h, followed by staining with primary antibodies against SDCCAG3, IFT20 or acetylated tubulin overnight at 4 °C. After 3 washes with PBS-T, samples were incubated with secondary Alexa Fluor dye–conjugated antibodies for 1 h at room temperature. Nuclei were stained with DAPI, and specimens mounted using Mowiol containing n-propyl gallate (Sigma-Aldrich). Images were captured using a Nikon Eclipse Ti-E inverted confocal microscope equipped with a 60x Plan Fluor oil immersion (1.4 NA) and 100x Plan Fluor oil immersion (1.45 NA) objectives. A series of digital optical sections (z-stacks) were captured using a Hamamatsu ORCA-Fusion Digital CMOS camera at room temperature, and 3D image reconstructions were produced. Images were processed and analyzed using Elements

AR 5.21 (Nikon), Adobe Illustrator and Photoshop software. Cilia length measurements were calculated from control (n=437 cilia, 3 mice) and *Pax3Cre-Dlg1*$^{F/F}$ (n=252 cilia from 4 mice). Ciliary levels of acetylated α-tubulin were derived from control (n=102 cilia) and *Pax3Cre-Dlg1*$^{F/F}$ (n=109 cilia). Total ciliary levels of SDCCAG3 and IFT20 were measured per cilium, and the data were calculated from: SDCCAG3 (n=105 cilia from 3 control mice and n=110 from 4 *Pax3Cre-Dlg1*$^{F/F}$ mice); IFT20 (n=99 cilia from 3 control mice and n= 104 from 4 *Pax3Cre-Dlg1*$^{F/F}$ mice).

Quantitative Real-Time PCR (RT-qPCR). Isolation of total RNA was performed using the NucleoSpin RNA II kit (Macherey-Nagel, cat. # 740955.50) following the manufacturer's instructions. RNA was reverse-transcribed using Superscript III Reverse Transcriptase (Invitrogen, cat. #18080-044) and cDNA amplified by qPCR using SYBR Green (Applied Biosystems, cat. #4309155). The qPCR was conducted in triplicate using the QuantStudio 7 Flex Real-Time PCR system with the following steps: 95 °C for 10 min, 40 cycles of [95 °C for 30 sec, 60 °C for 1 min, 72 °C for 30 sec], 95 °C for 1 min. Primer sequences used in this study for RT-qPCR are listed in Table 1. mRNA levels were determined using the comparative threshold cycle (Ct) method, normalizing to GAPDH and 18S ribosomal RNA. The mRNA levels were expressed relative to that in WT mCCD cells.

Inhibition of DLG1. Acute inhibition of DLG1 was done using the dimeric peptides AVLX-144 (YGRKKRRQRRR-*N*PEG$_4$(IETDV)$_2$, Tat-*N*-dimer), ReTat-*N*-dimer (rrrqrrkkr-*N*PEG$_4$(IETDV)$_2$ containing a retroinverso Tat cell-penetrating sequence and the non-PDZ-binding control AVLX-144-AA (YGRKKRRQRRR-*N*PEG$_4$(IEADA)$_2$ containing alanine mutations in the dimeric region [52, 53]. Compounds were purchased from WuXi AppTec (Shanghai, China) as hydrochloride salts and purities were checked by mass-spectrometry. Prior to the inhibitor experiment, the WT mCCD cells were seeded on glass coverslips and allowed to reach 80% confluence. To promote ciliogenesis, the cells were subjected to a 24 h

starvation period using the starvation medium outlined previously. After 12 h of starvation, the medium was changed to the inhibitor-supplemented starvation medium and incubated for an additional 12 h. Subsequently, the cells were examined using IFM analysis.

Immunoprecipitation, SDS-PAGE, and western blot analysis. Immunoprecipitation in mCCD and HEK293T cells was carried out as described previously [98], except that the washing buffer contained 0.1% NP-40 instead of 0.5% NP-40. Input and pellet fractions were analyzed by SDS-PAGE and western blotting as described previously [98] by using antibodies and dilutions as listed in Table 1.

TGFβ stimulation assay. Following cell seeding and 24 h incubation with starvation medium, the cells were stimulated with 2 ng/mL recombinant human TGF-β1 (R&D Systems, cat. # 240-B) diluted in starvation medium for varying durations of 30, 60, 90, and 120 min or left untreated (0 min). The cells were later lysed for subsequent analysis using the aforementioned SDS-PAGE and western blotting. The antibodies and dilutions used for this analysis are listed in Table 1.

Quantitative image and statistical analysis. Using IFM images and Fiji software [99] we measured cilium length, frequency, and relative mean fluorescence intensity (MFI) of relevant antibody-labeled antigens at the cilium or ciliary base in WT, *Dlg1*$^{-/-}$ and rescue IMCD3 and mCCD lines. Unless otherwise stated, the results were confirmed in at least three independent biological replicates. Statistical analyses were performed using GraphPad Prism 10.0.1. For manual quantification of ciliary staining intensities of fluorescent images, the background-corrected MFI was normalized to relevant control cells/mice. The data was was cumulated and tested for Gaussian normality using either D'Agostino's K-squared test or Shapiro–Wilk test. If the data followed a normal distribution, the two-tailed, unpaired Student's t-test was used when comparing two groups, or one-way ANOVA followed by

Tukey's multiple comparison tests was used for comparing more than two groups. If the data did not follow a normal distribution, the nonparametric Mann-Whitney test was used when comparing two groups, or the Kruskal-Wallis test with Dunn's multiple pairwise comparison tests was used for comparing more than two groups. All quantitative data are presented as mean ± standard deviation unless otherwise specified. Differences were considered significant when the p-value was <0.05. ns, not significant; *, P<0.05; **, P<0.01; ***, P<0.001; ****, P<0.0001. Quantitative analysis of western blot data was done as described previously [98].

Automated image analysis and primary cilia intensity measurements. PC2 (Figure 5C and 5D) and SDCCAG3 (Figures 5E and 5F) intensity levels were measured in spinning disk fluorescence microscopy 3D image stacks of transwells-cultured cells acquired from WT, *Dlg1*$^{-/-}$, and rescue mCCD cell lines in three independent experiments, with a total of 15-25 images and 431-739 cells/cilia analyzed per condition. To minimize any bias and ensure experimental reproducibility, all intensity measurements were performed by a fully automated MATLAB script reporting the mean fluorescence intensity of the protein of interest inside subregions of the identified primary cilia. The functional steps of the script are reported below. First, 1) Nucleus regions were automatically identified (DAPI channel, Gaussian filtering, background subtraction and global thresholding) and 2) primary cilia were accurately segmented (cilia marker channel, Gaussian filtering, and local thresholding) as the brightest 3D objects overlapping a nucleus region. Next, 3) primary cilium bases were identified as the closest cilium voxel to the center of mass of the corresponding nucleus region (assuming an outward growth of the cilia), and 4) primary cilium base regions were defined as the set of cilium voxels within a maximum (user defined) geodesic distance to the corresponding base. Finally, 5) SDCCAG3 and PC2 channels mean intensities were individually measured and reported inside each primary cilium, primary cilium base region,

and primary cilium body (whole cilium excluding the base region) after background intensity correction (3D median filtered image subtraction). Example images are shown in Figure S8. The script was developed for this project by Danish Bioimaging Infrastructure Image Analysis Core Facility (DBI-INFRA IACFF) and is available upon request and will soon be available from https://github.com/DBI-INFRA.

AlphaFold modeling of protein complexes. Structures of protein complexes shown in Figures 7C and S7B-D were modeled using a local installation of Alphafold v2.1.0 [60, 100] using sequences for *Mus musculus* (Mm) or *Homo sapiens* (Hs) DLG1, SDCCAG3, IFT20, and IFT54. Predicted interacting areas were inspected for a low Predicted Alignment Error (PAE) score as the main indicator for confidence. All figures of protein structures were prepared using PyMOL v. 2.5 (Schrodinger LLC, https://pymol.org).

Acknowledgments

We thank Søren L. Johansen and Maria S. Holm for expert technical assistance, and Pernille M. H. Olesen, Julie K. T. Sørensen, Søren Bjerg, and Maaryah Iqbal for contributing to the initial stages of this project, and Rachel Giles for helpful discussions and for contributing results that ended up not being included. We are grateful to the Polycystic Kidney Disease Research Resource Consortium (U54DK126114) for providing the anti-PC2 (rabbit polyclonal) antibody, and to Eric Féraille, Greg Pazour, Christopher Westlake, Kay Oliver Schink, Carlo Rivolta, and Michael Taschner for other reagents. This work was supported by grants NNF18SA0032928 and NNF22OC0080406 from the Novo Nordisk Foundation (LBP, SFP), grant 2032-00115B and 3103-00177B from the Independent Research Fund Denmark (LBP, STC), grant R01-DK108005 from the National Institute of Diabetes and Digestive and Kidney Diseases (MRM), the European Union's Horizon 2020 research and innovation program Marie Sklodowska-Curie Innovative Training Networks (ITN) grant 861329 (RR, RBR, KB, STC, LBP), and the Wellcome Trust grant 201585/B/18/Z (GDD, RBR).

Figure legends

Figure 1. Loss of *Dlg1* in mouse kidney cells leads to elongated cilia. (A) H&E staining of representative kidney sections from wildtype and *Pax3Cre-Dlg1*$^{F/F}$ mice. Black box denotes regions shown as magnified images on the right. Yellow arrows point to cystic tubules in the cortical region. **(B**, **C, D)** Immunofluorescence staining for cilia (acetylated α-tubulin, yellow) and quantification of ciliary length (**C**) and ciliary acetylated α-tubulin intensity (**D**) in kidney sections of wildtype (n=3) and *Pax3Cre-Dlg1*$^{F/F}$ (n=4) mice at 4 months of age. * denotes P<0.05. (**E**) Representative image of transwell filter-grown mCCD cell lines (mCh-DLG1: mCherry-DLG1). Cilia were visualized using acetylated tubulin antibody (AcTub, magenta), cell-cell contacts were visualized with E-cadherin antibody (green) and nuclei were stained with DAPI (blue). (**F**) Western blot analysis of total cell lysates of the indicated mCCD cells lines using antibodies against DLG1 and GAPDH (loading control). Molecular mass markers are shown in kDa to the left. (**G**, **H**) Quantification of ciliary length (**G**) and frequency (**H**) in the indicated transwell filter-grown mCCD lines. Ciliary length and ciliation rate was measured using the fully automated MATLAB script. Graphs represent accumulated data from three individual experiments, and statistical analysis was performed using Mann-Whitney U test (unpaired, two-tailed).

Figure 2. Analysis of cilia mass spectrometry results. (**A**) Volcano plot visualizing differential protein expression in the ciliary proteome upon disruption of DLG1. The proteins are colored according to their significance tier (Tier 1, 2, 3, and non-significant (NS)). The total amount of affected candidate ciliary proteins found in Tier 1 upon *Dlg1* depletion are highlighted on the right side of the volcano plot, while the proteins related to this research are marked on the volcano plot. The complete list of identified proteins can be found in Supplementary Table S1. Note that there are multiple points with the same x-axis values on

either side of the plot. These proteins were the ones where the median intensity values for either the WT or *Dlg1*$^{-/-}$ were 0. As a result, the log 2 ratio was infinite and we introduced a pseudo-value that is two units above or below the maximum and minimum ratio value across all genes respectively, to allow plotting of these points. (**B**, **C**) Gene Ontology enrichment analysis for biological process (**B**) and cellular component (**C**) using the proteins found in Tier1. The tables show the top 15 terms that are significantly enriched (Fisher's exact test value ≤0.05) and are listed in order of their enrichment ratio along with the corresponding GO terms.

Figure 3. Loss of DLG1 impairs ciliary localization of SDCCAG3 in IMCD3 and mCCD cells. (**A, E**) IFM analysis of ciliated cilia-BioID2 IMCD3 (**A**) and mCCD (**E**) cell lines showing comparative SDCCAG3 staining (green) in WT, *Dlg1*$^{-/-}$ and mCherry-DLG1 (mCh-DLG1) rescue cells. Cilia were stained with antibodies against acetylated α-tubulin (AcTub, magenta), and nuclei visualized with DAPI staining (blue). Insets show enlarged images of cilia, asterisks mark the ciliary base. The merged insets show primary cilia with channels shifted to aid visualization. (**B**, **F**) Quantification of the relative mean fluorescence intensity (MFI) of SDCCAG3 staining along the cilium of cilia-BioID2 IMCD3 cell lines (**B**) or at the ciliary base of mCCD cell lines (**F**). Graphs represent WT normalized and accumulated data (n=3). Kruskal-Wallis test with Dunn's multiple comparison test was used for the statistical analysis. (**C**, **D**, **G**) Western blot analysis of total cell lysates of cilia-BioID2 IMCD3 (**C**, **D**) or mCCD (**G**) cell lines. Blots were probed with antibodies as indicated, GAPDH was used as loading control. Molecular mass markers are shown in kDa to the left.

Figure 4. Conditional loss of DLG1 in mouse kidney leads to impaired ciliary localization of SDCCAG3 and IFT20. (**A**, **B**) Immunofluorescence staining of SDCCAG3 (**A**) or IFT20 (**B**), both in yellow, and acetylated α-tubulin (AcTub, magenta) in kidney sections from wildtype and *Pax3Cre-Dlg1*$^{F/F}$ mice. (**C**) Quantification of relative MFI of

SDCCAG3 and IFT20 in cilia of wildtype (n=3) and *Pax3Cre-Dlg1*$^{F/F}$ (n=4) mice, respectively. The levels from control mice were set to 1, and the ciliary levels from mutant mice were compared to that (i.e., relative fluorescence intensity). Data shown are the average values from each mouse.

Figure 5. Loss of DLG1 affects ciliary composition in transwell filter-grown mCCD cells. (**A**, **B**) Representative top (**A**) and side view (**B**) confocal images of transwell filter-grown WT, *Dlg1*$^{-/-}$ and mCherry-DLG1 (mCh-DLG1) rescue lines. The cells were stained for E-cadherin (green) and PALS1 (magenta) to visualize the basolateral membrane and apical-lateral border, respectively. (**C**, **E**) IFM analysis of PC2 (**C**) or SDCCAG3 (**E**) (green) in transwell indicated cell lines. Cilia were visualized with antibody against acetylated tubulin (AcTub, magenta), and nuclei stained with DAPI (blue). Insets show enlarged images of cilia, while the merged insets show primary cilia with channels shifted to aid visualization. (**D, F**) Quantification of the relative MFI of PC2 (**D**) and SDCCAG3 (**F**) along the cilium (right panels) and at the ciliary base (left panels). The graphs represent normalized and accumulated data (n=3). The number of dots in each condition represents the number of primary cilia quantified. The MFI of SDCCAG3 or PC2 was measured using the fully automated MATLAB-based quantification. Statistical analysis utilized one-way ANOVA with Tukey's multiple comparison test.

Figure 6. A CAKUT-associated DLG1 missense variant fails to rescue ciliary phenotype of *Dlg1*$^{-/-}$ mCCD cells. (**A**) DLG1 protein domain structure and schematic representation and localization of the human CAKUT-associated DLG1^{T489R} variant and the rat counterpart (DLG1^{T507R}). The specific human WT DLG1 isoform depicted is DLG1-210 (UniProt Q12959-5), which is encoded by transcript ENST00000422288 (ensembl.org) [36] the corresponding WT rat DLG1 isoform is UniProt A0A8I6A5M7. (**B**) Western blot validation of stable expression of transgenic mutant mCherry-DLG1 (mCh-DLG1^{T507R}) in mCCD cells

767 using antibodies as indicated. (**C)** Ciliary length measurements of indicated cell lines, grown
768 on transwell filters (n=3). (**D**, **E**) IFM analysis of the indicated ciliated cell lines using
769 antibodies against SDCCAG3 (**D**) or IFT20 (**E**), both shown in green. Acetylated α-tubulin
770 (AcTub, magenta) was used to stain cilia; nuclei were visualized with DAPI (blue). Insets
771 show enlarged images of cilia, asterisks mark the ciliary base. **(F, G**) Quantification of
772 relative MFI of SDCCAG3 (**F**) and IFT20 (**G**) at the ciliary base of indicated mCCD cell
773 lines, based on images as shown in panels (**D**) and (**E**), respectively. Kruskal-Wallis test with
774 Dunn's multiple comparison test was used for statistical analysis (n=3). (**H**, **J**) Western blot
775 analysis of total or phosphorylated (p) SMAD2 (**H**) and TAK1 (**J**) upon stimulation with
776 TGFβ-1 ligand for indicated times in growth-arrested mCCD cells. (**I**, **K**) Quantifications of
777 protein phosphorylation shown in panels (**H**, **J**), respectively (n = 3).

778 **Figure 7. Analysis of DLG1, IFT20 and SDCCAG3 interactions.** (**A**, **B**)
779 Immunoprecipitation with anti-GFP beads was performed in HEK293T cells transiently
780 expressing FLAG-Myc-SDCCAG3 (**A**) or FLAG-IFT20 (HTF-IFT20) (**B**) together with the
781 indicated GFP-fusions. Input and pellet fractions were subjected to SDS-PAGE and western
782 blot analysis using antibodies against FLAG or GFP, as indicated, and GFP expressed alone
783 was used as negative control. Molecular mass markers are indicated in kDa to the left. (**C**)
784 Structural prediction for the complex between MmSDCCAG3 (yellow) and MmIFT20 (cyan)
785 in cartoon representation (upper panel). The structure is predicted to be an anti-parallel
786 hetero-dimer coiled coil. The lower panel includes IFT54 showing its binding to IFT20 is
787 mutually exclusive with binding of SDCCAG3 to IFT20. (**D**) Proposed model for how DLG1
788 promotes ciliary trafficking of SDCCAG3, IFT20 and PC2. Based on [7, 9] and data
789 presented in the current study. CRE, common recycling endosome.

790

Reagent type (species) or resource	Designation	Source or reference	Identifiers	Additional information
Kidney tissue (*Mus musculus*)	*Pax3-Cre* strain with *Dlg1*$^{+/+}$ alleles	[39]	Wild type	C57BL/6J-CBA/J mixed background
Kidney tissue (*Mus musculus*)	*Pax3-Cre* strain with *Dlg1*$^{F/F}$ alleles	[39]	*Pax3Cre-Dlg1*$^{F/F}$	C57BL/6J-CBA/J mixed background
Cell line (*Mus musculus*)	IMCD3 Flp-In	[45]	Wild type (parental)	
Cell line (*Mus musculus*)	IMCD3 Flp-In w/ cilia-BioID2	[45]	Wild type	
Cell line (*Mus musculus*)	IMCD3 Flp-In w/ BioID2	[45]	Wild type	
Cell line (*Mus musculus*)	mCCD	[101]	Wild type (parental)	cl1 parental cells
Cell line (*Homo sapiens*)	HEK293T	ATCC	Cat. #CRL-3216	
Cell line (*Mus musculus*)	IMCD3 Flp-In w/ DLG1-BioID2	This study	Pool	Generated by Flp-FRT recombination
Cell line (*Mus musculus*)	IMCD3 Flp-In w/ cilia-BioID2 *Dlg1*$^{-/-}$	This study	Pool of knockout	Generated by CRISPR/Cas9 methodology
Cell line (*Mus musculus*)	IMCD3 Flp-In w/ BioID2 *Dlg1*$^{-/-}$	This study	Pool of knockout	Generated by CRISPR/Cas9 methodology
Cell line (*Mus musculus*)	mCCD *Dlg1*$^{-/-}$	This study	Clone A8	Generated by CRISPR/Cas9 methodology
Cell line (*Mus musculus*)	IMCD3 Flp-In w/ cilia-BioID2 *Dlg1*$^{-/-}$ w/ mCherry-DLG1	This study	Pool/rescue line	Generated by lentiviral transduction
Cell line (*Mus musculus*)	mCCD *Dlg1*$^{-/-}$ w/ mCherry-DLG1	This study	Pool/rescue line	Generated by lentiviral transduction
Cell line (*Mus musculus*)	mCCD *Dlg1*$^{-/-}$ w/ mCherry-DLG1^{T507R}	This study	Pool/mutant line	Generated by lentiviral transduction
Cell line (*Homo sapiens*)	hTERT-RPE1 w/SMO-tRFP	[89]	RPE1 SMO-tRFP	
Strain, strain	DH10B	Lab stock	N/A	

background (*Escherichia coli*)				
Sequence-based reagent	*M. musculus Dlg1* exon 5 sgRNA target sequence	Eurofins Genomics	sgRNA 1	5'-TTCTCCACAAGTCACAAATG-3'
Sequence-based reagent	*M. musculus Dlg1* exon 8 sgRNA target sequence	Eurofins Genomics	sgRNA 2	5'-TTGAGTCATCTCCAATGTGT-3'
Sequence-based reagent	*M. musculus Dlg1* exon 9 sgRNA target sequence	Eurofins Genomics	sgRNA 3	5'-TGCGATTGTATGTGAAAAGG-3'
Sequence-based reagent	*M. musculus Dlg1* exon 14 sgRNA target sequence	Eurofins Genomics	sgRNA 4	5'-GGGTCGATATTGCGCAACGA-3'
Sequence-based reagent	*M. musculus Gapdh* RT-qPCR primer sequence	Eurofins Genomics	N/A	sense 5'-TGTCCGTCGTGGATCTGAC-3'; antisense 5'-CCTGCTTCACCACCTTCTTG-3'
Sequence-based reagent	*M. musculus 18S rRNA* RT-qPCR primer sequence	Eurofins Genomics	N/A	sense 5'-GCAATTATTCCCCATGAACG-3'; antisense 5'-AGGGCCTCACTAAACCATCC-3'
Sequence-based reagent	*M. musculus Dlg1* RT-qPCR primer sequence	Eurofins Genomics	N/A	sense 5'-CGAAGAACAGTCTGGGCCTT-3'; antisense 5'-GGGGATCTGTGTCAGTGTGG-3'
Sequence-based reagent	*M. musculus Dlg2* RT-qPCR primer sequence	Eurofins Genomics	N/A	sense 5'-TGCCTGGCTGGAGTTTACAG-3'; antisense 5'-TTTTACAATGGGGCCTCCGC-3'
Sequence-based reagent	*M. musculus Dlg3* RT-qPCR primer sequence	Eurofins Genomics	N/A	sense 5'-GAGCCAGTGACACGACAAGA-3'; antisense 5'-GCGGGAACTCAGAGATGAGG-3'
Sequence-based reagent	*M. musculus Dlg4* RT-qPCR primer sequence	Eurofins Genomics	N/A	sense 5'-GGGCCTAAAGGACTTGGCTT-3'; antisense 5'-TGACATCCTCTAGCCCCACA-3'
Sequence-based reagent	*Rattus norvegicus Dlg1* PCR primer	Eurofins Genomics	rDLG1.kpnI	5'-CCGGTACCCCGGTCCGGAAGCAAGATAC-3'
Sequence-based	*Rattus norvegicus Dlg1* PCR primer	Eurofins Genomics	rDLG1.notI	5'-CCGCGGCCGCTCATAATT

reagent				TTTCTTTTGCTGGGACCC AG -3’
DNA plasmid	pSpCas9(BB)-2A-Puro (PX459) V2.0	Addgene	Cat. #62988, pSpCas9	Expression vector, CRISPR
DNA plasmid	gRNA 1/pSpCas9	This study	pSpCas9-gRNA 1	Expression vector, CRISPR
DNA plasmid	gRNA 2/pSpCas9	This study	pSpCas9-gRNA 2	Expression vector, CRISPR
DNA plasmid	gRNA 3/pSpCas9	This study	pSpCas9-gRNA 3	Expression vector, CRISPR
DNA plasmid	gRNA 4/pSpCas9	This study	pSpCas9-gRNA 4	Expression vector, CRISPR
DNA plasmid	*Mus musculus* SDCCAG3/ pCMV6-Myc-DDK	Origene	Cat. #MR217984, FLAG-MYC-SDCCAG3	Expression vector
DNA plasmid	*Homo sapiens* IFT20/ pcDNA5.1-6xHis-3xFLAG-TEV	Made by Michael Tascher from Esben Lorentzen’s lab using standard approaches as in [61]	HFT-IFT20	Expression vector
DNA plasmid	pEGFP-C1	Clontech	eGFP	Expression vector
DNA plasmid	*Mus musculus* IFT20/ pEGFP-N1	[13]	IFT20-eGFP	Expression vector
DNA plasmid	*Rattus norvegicus* DLG1/pEGFP-C1	[92]	eGFP-DLG1	Expression vector, DLG1 insert is isolated from rat brain [93]
DNA plasmid	pENTR220-mCherry-C1	[93]	N/A	Gateway entry vector
DNA plasmid	pCDH-EF1a-Gateway-IRES-BLAST	[93]	pCHD	Gateway destination vector for generating lentiviral expression vector
DNA plasmid	pMD2.G	[98]	N/A	Lentiviral packaging vector
DNA plasmid	pCMVΔ-R8.2	[98]	N/A	Lentiviral packaging vector
DNA plasmid	*Rattus norvegicus* DLG1/pENTR220-mCherry-C1	This study	pENTR220-mCherry-DLG1	Gateway entry vector, cloned in KpnI and NotI sites
DNA plasmid	*Rattus norvegicus* mCherry-DLG1/ pCDH-EF1a-Gateway-IRES-BLAST	This study	pCDH-mCherry-DLG1	Lentiviral expression vector, generated with Gateway LR reaction using pENTR220-mCherry-DLG1 and pCDH plasmids
DNA plasmid	*Rattus norvegicus* mCherry-	This study	pCDH-mCherry-	Lentiviral expression vector, Generated by GenScript

	DLG1^{T507R}/ pCDH-EF1a-Gateway-IRES-BLAST		DLG1^{T507R}	
Antibody	Anti-alpha-tubulin (mouse monoclonal)	Sigma-Aldrich	Cat. #T5168	WB (1:10000)
Antibody	Anti-acetylated alpha-tubulin (mouse monoclonal)	Sigma-Aldrich	Cat. #T7451	IFM (1:2000) IHC (1:2000)
Antibody	Anti-acetylated alpha-tubulin (rabbit monoclonal)	Abcam	Cat. #ab179484	IFM (1:2000)
Antibody	Anti-ARL13B (rabbit polyclonal)	Proteintech	Cat. #17711-1-AP	IFM (1:500)
Antibody	Anti-DLG1 (rabbit polyclonal)	Abcam	Cat. #ab300481	IFM (1:750) WB (1:1000)
Antibody	Anti-DLG1 (rabbit polyclonal)	Thermo Scientific	Cat. #PA1-741	WB (1:600)
Antibody	Anti-E-Cadherin (rabbit polyclonal)	Cell Signaling Technology	Cat. # 3195	IFM (1:1000)
Antibody	Anti-FLAG (mouse monoclonal)	Sigma-Aldrich	Cat. #F1804	WB (1:1000)
Antibody	Anti-GAPDH (rabbit polyclonal)	Cell Signaling Technology	Cat. #2118	WB (1:1000)
Antibody	Anti-GFP (chicken polyclonal)	Abcam	Cat. #ab13970	WB (1:1000)
Antibody	Anti-GFP (rabbit polyclonal)	Sigma-Aldrich	Cat. #SAB4301138	WB (1:500)
Antibody	Anti-IFT20 (rabbit polyclonal)	Proteintech	Cat. #13615-1-AP	IFM (1:200) IHC (1:100) WB (1:500)
Antibody	Anti-PALS1 (mouse monoclonal)	Santa Cruz Biotechnology	Cat. #sc-365411	IFM (1:1000)
Antibody	Anti-PC2 (rabbit polyclonal)	PKD Research Resource Consortium	N/A	IFM (1:1000) WB (1:600)
Antibody	Anti-PC2 (mouse monoclonal)	Santa Cruz Biotechnology	Cat. #sc-28331	IFM (1:500) WB (1:1000)
Antibody	Anti-SDCCAG3 (rabbit polyclonal)	Proteintech	Cat. #15969-1-AP	IFM (1:600) IHC (1:100) WB (1:1000)

Antibody	Anti-SMAD2 (rabbit polyclonal)	Cell Signaling Technology	Cat. #5339	WB (1:200)
Antibody	Anti-pSMAD2$^{Ser465/467}$ (rabbit polyclonal)	Cell Signaling Technology	Cat. #3108	WB (1:200)
Antibody	Anti-rSEC8 (mouse monoclonal)	Enzo Life Sciences	Cat. #ADI-VAM-SV016	IFM (1:1000) WB (1:2000)
Antibody	Anti-TAK1 (rabbit polyclonal)	Cell Signaling Technology	Cat. #4505	WB (1:300)
Antibody	Anti-pTAK1^{Ser412} (mouse monoclonal)	Bioss Antibodies	Cat. #bs-3435R	WB (1:200)
Antibody	Anti-pTAK1$^{Thr184/187}$ (mouse monoclonal)	Bioss Antibodies	Cat. #bs-3439R	WB (1:200)
Antibody	Anti-Mouse-AF488 (donkey polyclonal)	Invitrogen	Cat. #A-21202	IFM (1:600)
Antibody	Anti-Mouse-AF568 (donkey polyclonal)	Invitrogen	Cat. # A-10037	IFM (1:600)
Antibody	Anti-Rabbit-AF488 (donkey polyclonal)	Invitrogen	Cat. # A-21206	IFM (1:600)
Antibody	Anti-Rabbit-AF568 (donkey polyclonal)	Invitrogen	Cat. #A-10042	IFM (1:600)
Antibody	Anti-Chicken-HRP (goat polyclonal)	Invitrogen	Cat. #A-16054	WB (1:6000)
Antibody	Anti-Mouse-HRP (goat polyclonal)	Agilent Technologies, Inc.	Cat. #P0447	WB (1:10000)
Antibody	Anti-Rabbit-HRP (swine polyclonal)	Agilent Technologies, Inc.	Cat. #P0399	WB (1:10000)
Peptide inhibitor	DLG-specific inhibitor	WuXi AppTtec (Shanghai, China)	AVLX-144	Tat-N-dimer; described in [52, 53]
Peptide inhibitor	DLG-specific inhibitor	WuXi AppTtec (Shanghai, China)	Re-Tat-N-dimer	Described in [52, 53]
Peptide inhibitor	non-PDZ-binding control	WuXi AppTec (Shanghai, China)	AVLX-144-AA	Described in [52, 53]

Secondary detection	Streptavidin, Alexa Fluor 488 Conjugate	Invitrogen	Cat. #S32354	IFM (1:1000)
Fluorescent stain	DAPI	Sigma Aldrich	Cat. #D9542	IFM (1:5000)

Table 1. Cell lines and reagents used in this study. N/A, not applicable; WB, western blot; IHC, immunohistochemistry.

References

1. Mill, P., S.T. Christensen, and L.B. Pedersen, *Primary cilia as dynamic and diverse signalling hubs in development and disease.* Nat Rev Genet, 2023. **24**(7): p. 421-441.
2. Pazour, G.J., et al., *Polycystin-2 localizes to kidney cilia and the ciliary level is elevated in orpk mice with polycystic kidney disease.* Curr Biol, 2002. **12**(11): p. R378-80.
3. Yoder, B.K., X. Hou, and L.M. Guay-Woodford, *The polycystic kidney disease proteins, polycystin-1, polycystin-2, polaris, and cystin, are co-localized in renal cilia.* J Am Soc Nephrol, 2002. **13**(10): p. 2508-16.
4. Ma, M., A.R. Gallagher, and S. Somlo, *Ciliary Mechanisms of Cyst Formation in Polycystic Kidney Disease.* Cold Spring Harb Perspect Biol, 2017. **9**(11).
5. Cantero, M.D.R. and H.F. Cantiello, *Polycystin-2 (TRPP2): Ion channel properties and regulation.* Gene, 2022. **827**: p. 146313.
6. Walker, R.V., et al., *Ciliary exclusion of Polycystin-2 promotes kidney cystogenesis in an autosomal dominant polycystic kidney disease model.* Nat Commun, 2019. **10**(1): p. 4072.
7. Monis, W.J., V. Faundez, and G.J. Pazour, *BLOC-1 is required for selective membrane protein trafficking from endosomes to primary cilia.* J Cell Biol, 2017. **216**(7): p. 2131-2150.
8. Nachury, M.V., *The molecular machines that traffic signaling receptors into and out of cilia.* Curr Opin Cell Biol, 2018. **51**: p. 124-131.
9. Hu, J. and P.C. Harris, *Regulation of polycystin expression, maturation and trafficking.* Cell Signal, 2020. **72**: p. 109630.
10. Stoops, E.H. and M.J. Caplan, *Trafficking to the apical and basolateral membranes in polarized epithelial cells.* J Am Soc Nephrol, 2014. **25**(7): p. 1375-86.

820 11. Hoffmeister, H., et al., *Polycystin-2 takes different routes to the somatic and ciliary*
821 *plasma membrane.* J Cell Biol, 2011. **192**(4): p. 631-45.
822 12. Kim, H., et al., *Ciliary membrane proteins traffic through the Golgi via a*
823 *Rabep1/GGA1/Arl3-dependent mechanism.* Nat Commun, 2014. **5**: p. 5482.
824 13. Follit, J.A., et al., *The intraflagellar transport protein IFT20 is associated with the*
825 *Golgi complex and is required for cilia assembly.* Mol Biol Cell, 2006. **17**(9): p.
826 3781-92.
827 14. Follit, J.A., et al., *The Golgin GMAP210/TRIP11 anchors IFT20 to the Golgi*
828 *complex.* PLoS Genet, 2008. **4**(12): p. e1000315.
829 15. Yu, F., et al., *The serologically defined colon cancer antigen-3 (SDCCAG3) is*
830 *involved in the regulation of ciliogenesis.* Sci Rep, 2016. **6**: p. 35399.
831 16. Tilley, F.C., et al., *Retromer associates with the cytoplasmic amino-terminus of*
832 *polycystin-2.* J Cell Sci, 2018. **131**(11).
833 17. Funke, L., S. Dakoji, and D.S. Bredt, *Membrane-associated guanylate kinases*
834 *regulate adhesion and plasticity at cell junctions.* Annu Rev Biochem, 2005. **74**: p.
835 219-45.
836 18. Lickert, H. and C.A. Van Campenhout, *Evolution of the Discs large gene family*
837 *provides new insights into the establishment of apical epithelial polarity and the*
838 *etiology of mental retardation.* Commun Integr Biol, 2012. **5**(3): p. 287-90.
839 19. Mauceri, D., et al., *Dual role of CaMKII-dependent SAP97 phosphorylation in*
840 *mediating trafficking and insertion of NMDA receptor subunit NR2A.* J Neurochem,
841 2007. **100**(4): p. 1032-46.
842 20. Gardoni, F., et al., *SAP97 directs the localization of Kv4.2 to spines in hippocampal*
843 *neurons: regulation by CaMKII.* J Biol Chem, 2007. **282**(39): p. 28691-28699.

21. Tiffany, A.M., et al., *PSD-95 and SAP97 Exhibit Distinct Mechanisms for Regulating K ⍰ Channel Surface Expression and Clustering.* J Cell Biol, 2000. **148**(1): p. 147-58.

22. Sans, N., et al., *Synapse-Associated Protein 97 Selectively Associates with a Subset of AMPA Receptors Early in their Biosynthetic Pathway.* J Neurosci, 2001. **21**(19): p. 7506-16.

23. van Ree, J.H., et al., *Pten regulates spindle pole movement through Dlg1-mediated recruitment of Eg5 to centrosomes.* Nat Cell Biol, 2016. **18**(7): p. 814-21.

24. Mick, D.U., et al., *Proteomics of Primary Cilia by Proximity Labeling.* Dev Cell, 2015. **35**(4): p. 497-512.

25. Kohli, P., et al., *The ciliary membrane-associated proteome reveals actin-binding proteins as key components of cilia.* EMBO Rep, 2017. **18**(9): p. 1521-1535.

26. Datta, P., et al., *Accumulation of non-outer segment proteins in the outer segment underlies photoreceptor degeneration in Bardet-Biedl syndrome.* Proc Natl Acad Sci U S A, 2015. **112**(32): p. E4400-9.

27. Hanada, T., et al., *GAKIN, a novel kinesin-like protein associates with the human homologue of the Drosophila discs large tumor suppressor in T lymphocytes.* J Biol Chem, 2000. **275**(37): p. 28774-84.

28. Schou, K.B., et al., *KIF13B establishes a CAV1-enriched microdomain at the ciliary transition zone to promote Sonic hedgehog signaling.* Nature Communications, 2017. **8**: p. 14177.

29. Juhl, A.D., et al., *Transient accumulation and bidirectional movement of KIF13B in primary cilia.* J Cell Sci, 2023. **136**(5).

30. Caruana, G. and A. Bernstein, *Craniofacial dysmorphogenesis including cleft palate in mice with an insertional mutation in the discs large gene.* Mol Cell Biol, 2001. **21**(5): p. 1475-83.

869 31. Naim, E., et al., *Mutagenesis of the epithelial polarity gene, discs large 1, perturbs*
870 *nephrogenesis in the developing mouse kidney*. Kidney Int, 2005. **68**(3): p. 955-65.
871 32. Mahoney, Z.X., et al., *Discs-large homolog 1 regulates smooth muscle orientation in*
872 *the mouse ureter*. PNAS, 2006. **103**(52): p. 19872-7.
873 33. Iizuka-Kogo, A., et al., *Abnormal development of urogenital organs in Dlgh1-*
874 *deficient mice*. Development, 2007. **134**(9): p. 1799-807.
875 34. Ahn, S., et al., *Scaffolding Proteins DLG1 and CASK Cooperate to Maintain the*
876 *Nephron Progenitor Population during Kidney Development.* J Am Soc Nephrol,
877 2013. **24**: p. 1127–1138.
878 35. Westland, R., et al., *Copy number variation analysis identifies novel CAKUT*
879 *candidate genes in children with a solitary functioning kidney.* Kidney Int, 2015.
880 **88**(6): p. 1402-1410.
881 36. Nicolaou, N., et al., *Prioritization and burden analysis of rare variants in 208*
882 *candidate genes suggest they do not play a major role in CAKUT.* Kidney Int, 2016.
883 **89**(2): p. 476-86.
884 37. Willatt, L., et al., *3q29 microdeletion syndrome: clinical and molecular*
885 *characterization of a new syndrome.* Am J Hum Genet, 2005. **77**(1): p. 154-60.
886 38. Gabriel, G.C., G.J. Pazour, and C.W. Lo, *Congenital Heart Defects and Ciliopathies*
887 *Associated With Renal Phenotypes.* Front Pediatr, 2018. **6**: p. 175.
888 39. Kim, S.T., et al., *DLG1 influences distal ureter maturation via a non-epithelial cell*
889 *autonomous mechanism involving reduced retinoic acid signaling, Ret expression,*
890 *and apoptosis*. Dev Biol, 2014. **390**(2): p. 160-9.
891 40. Montesano, R., et al., *cAMP-dependent chloride secretion mediates tubule*
892 *enlargement and cyst formation by cultured mammalian collecting duct cells.* Am J
893 Physiol Renal Physiol, 2009. **296**(2): p. F446-57.

894 41. Pedersen, L.B., et al., *The ciliary cytoskeleton*. Compr Physiol, 2012. **2**(1): p. 779-
895 803.
896 42. Avasthi, P. and W.F. Marshall, *Stages of ciliogenesis and regulation of ciliary length.*
897 Differentiation, 2012. **83**(2): p. S30-42.
898 43. Liu, X., et al., *Polycystin-2 is an essential ion channel subunit in the primary cilium of*
899 *the renal collecting duct epithelium.* Elife, 2018. **7**.
900 44. Shao, L., et al., *Genetic reduction of cilium length by targeting intraflagellar*
901 *transport 88 protein impedes kidney and liver cyst formation in mouse models of*
902 *autosomal polycystic kidney disease.* Kidney Int, 2020. **98**(5): p. 1225-1241.
903 45. Aslanyan, M.G., et al., *A targeted multi-proteomics approach generates a blueprint of*
904 *the ciliary ubiquitinome.* Front Cell Dev Biol, 2023. **11**: p. 1113656.
905 46. McGough, I.J., et al., *Identification of molecular heterogeneity in SNX27-retromer-*
906 *mediated endosome-to-plasma-membrane recycling.* J Cell Sci, 2014. **127**(Pt 22): p.
907 4940-53.
908 47. Cole, D.G., et al., *Chlamydomonas kinesin-II-dependent intraflagellar transport*
909 *(IFT): IFT particles contain proteins required for ciliary assembly in Caenorhabditis*
910 *elegans sensory neurons*. J Cell Biol, 1998. **141**: p. 993-1008.
911 48. Inoue, M., et al., *Compartmentalization of the exocyst complex in lipid rafts controls*
912 *Glut4 vesicle tethering.* Mol Biol Cell, 2006. **17**(5): p. 2303-11.
913 49. Bolis, A., et al., *Dlg1, Sec8, and Mtmr2 regulate membrane homeostasis in Schwann*
914 *cell myelination.* J Neurosci, 2009. **29**(27): p. 8858-70.
915 50. Fogelgren, B., et al., *The exocyst protein Sec10 interacts with Polycystin-2 and*
916 *knockdown causes PKD-phenotypes.* PLoS Genet, 2011. **7**(4): p. e1001361.
917 51. Seixas, C., et al., *Arl13b and the exocyst interact synergistically in ciliogenesis.* Mol
918 Biol Cell, 2016. **27**(2): p. 308-20.

52. Bach, A., et al., *A high-affinity, dimeric inhibitor of PSD-95 bivalently interacts with PDZ1-2 and protects against ischemic brain damage*. Proc Natl Acad Sci U S A, 2012. **109**(9): p. 3317-22.

53. Bach, A., et al., *Modified Peptides as Potent Inhibitors of the Postsynaptic Density-95/N-Methyl-D-Aspartate Receptor Interaction*. J Med Chem, 2008. **51**(20): p. 6450–6459.

54. Unno, K., T. Hanada, and A.H. Chishti, *Functional involvement of human discs large tumor suppressor in cytokinesis*. Exp Cell Res, 2008. **314**(17): p. 3118-29.

55. Bernabe-Rubio, M., et al., *Novel role for the midbody in primary ciliogenesis by polarized epithelial cells*. J Cell Biol, 2016. **214**(3): p. 259-73.

56. Choi, M.E., Y. Ding, and S.I. Kim, *TGF-beta signaling via TAK1 pathway: role in kidney fibrosis*. Semin Nephrol, 2012. **32**(3): p. 244-52.

57. Sureshbabu, A., S.A. Muhsin, and M.E. Choi, *TGF-beta signaling in the kidney: profibrotic and protective effects*. Am J Physiol Renal Physiol, 2016. **310**(7): p. F596-F606.

58. Clement, C.A., et al., *Regulation of TGFβ signaling by endocytosis at the pocket region of the primary cilium* Cell Rep, 2013. **3**: p. 1806-1814.

59. Christensen, S.T., et al., *Primary Cilia and Coordination of Receptor Tyrosine Kinase (RTK) and Transforming Growth Factor beta (TGF-beta) Signaling*. Cold Spring Harb Perspect Biol, 2017. **9**(6).

60. Jumper, J., et al., *Highly accurate protein structure prediction with AlphaFold*. Nature, 2021. **596**(7873): p. 583-589.

61. Taschner, M., et al., *Intraflagellar transport proteins 172, 80, 57, 54, 38, and 20 form a stable tubulin-binding IFT-B2 complex*. EMBO J, 2016. **35**(7): p. 773-90.

943 62. Nazarian, R., et al., *Reinvestigation of the dysbindin subunit of BLOC-1 (biogenesis of*
944 *lysosome-related organelles complex-1) as a dystrobrevin-binding protein.* Biochem
945 J, 2006. **395**(3): p. 587-98.
946 63. Kanai, Y., D. Wang, and N. Hirokawa, *KIF13B enhances the endocytosis of LRP1 by*
947 *recruiting LRP1 to caveolae*. J Cell Biol, 2014. **204**(3): p. 395-408.
948 64. Morthorst, S.K., et al., *Angiomotin isoform 2 promotes binding of PALS1 to KIF13B*
949 *at primary cilia and regulates ciliary length and signaling.* J Cell Sci, 2022. **135**(12).
950 65. Huttlin, E.L., et al., *Dual proteome-scale networks reveal cell-specific remodeling of*
951 *the human interactome.* Cell, 2021. **184**(11): p. 3022-3040 e28.
952 66. Mochizuki, T., et al., *PKD2, a Gene for Polycystic Kidney Disease That Encodes an*
953 *Integral Membrane Protein.* Science, 1996. **272**(5266): p. 1339-42.
954 67. Heider, M.R. and M. Munson, *Exorcising the exocyst complex.* Traffic, 2012. **13**(7):
955 p. 898-907.
956 68. Yamanaka, T. and S. Ohno, *Role of Lgl/Dlg/Scribble in the regulation of epithelial*
957 *junction, polarity and growth.* Front Biosci, 2008. **1**(13): p. 6693-707.
958 69. Osterweil, E., D.G. Wells, and M.S. Mooseker, *A role for myosin VI in postsynaptic*
959 *structure and glutamate receptor endocytosis.* J Cell Biol, 2005. **168**(2): p. 329-38.
960 70. de Vreede, G., et al., *The Scribble module regulates retromer-dependent endocytic*
961 *trafficking during epithelial polarization.* Development, 2014. **141**(14): p. 2796-802.
962 71. Wang, P., et al., *SNX17 Recruits USP9X to Antagonize MIB1-Mediated*
963 *Ubiquitination and Degradation of PCM1 during Serum-Starvation-Induced*
964 *Ciliogenesis.* Cells, 2019. **8**(11).
965 72. Severin, M., et al., *Dynamic localization of the Na+-HCO3- co-transporter NBCn1 to*
966 *the plasma membrane, centrosomes, spindle and primary cilia.* J Cell Sci, 2023.
967 **136**(7).

968 73. Olesen, C.W., et al., *Trafficking, localization and degradation of the Na(+),HCO(3)(-*
969 *) co-transporter NBCn1 in kidney and breast epithelial cells.* Sci Rep, 2018. **8**(1): p.
970 7435.
971 74. Mellman, I. and W.J. Nelson, *Coordinated protein sorting, targeting and distribution*
972 *in polarized cells.* Nat Rev Mol Cell Biol, 2008. **9**(11): p. 833-45.
973 75. Akhmanova, A. and L.C. Kapitein, *Mechanisms of microtubule organization in*
974 *differentiated animal cells.* Nat Rev Mol Cell Biol, 2022. **23**(8): p. 541-558.
975 76. Sang, L., et al., *Mapping the NPHP-JBTS-MKS protein network reveals ciliopathy*
976 *disease genes and pathways.* Cell, 2011. **145**(4): p. 513-28.
977 77. Delous, M., et al., *Nephrocystin-1 and nephrocystin-4 are required for epithelial*
978 *morphogenesis and associate with PALS1/PATJ and Par6.* Hum Mol Genet, 2009.
979 **18**(24): p. 4711-23.
980 78. Tan, B., et al., *The Mammalian Crumbs Complex Defines a Distinct Polarity Domain*
981 *Apical of Epithelial Tight Junctions.* Curr Biol, 2020. **30**(14): p. 2791-2804 e6.
982 79. Fan, S., et al., *Polarity proteins control ciliogenesis via kinesin motor interactions.*
983 Curr Biol, 2004. **14**(16): p. 1451-61.
984 80. Bazellieres, E., et al., *Role of the Crumbs proteins in ciliogenesis, cell migration and*
985 *actin organization.* Semin Cell Dev Biol, 2018. **81**: p. 13-20.
986 81. Duning, K., et al., *Polycystin-2 activity is controlled by transcriptional coactivator*
987 *with PDZ binding motif and PALS1-associated tight junction protein.* J Biol Chem,
988 2010. **285**(44): p. 33584-8.
989 82. Kim, S.I. and M.E. Choi, *TGF-beta-activated kinase-1: New insights into the*
990 *mechanism of TGF-beta signaling and kidney disease.* Kidney Res Clin Pract, 2012.
991 **31**(2): p. 94-105.

992 83. Peng, Z., et al., *Dlg1 Knockout Inhibits Microglial Activation and Alleviates*
993 *Lipopolysaccharide-Induced Depression-Like Behavior in Mice.* Neurosci Bull, 2021.
994 **37**(12): p. 1671-1682.
995 84. Podrini, C., L. Cassina, and A. Boletta, *Metabolic reprogramming and the role of*
996 *mitochondria in polycystic kidney disease.* Cell Signal, 2020. **67**: p. 109495.
997 85. Steidl, M.E., et al., *Primary cilia sense glutamine availability and respond via*
998 *asparagine synthetase.* Nat Metab, 2023. **5**(3): p. 385-397.
999 86. Walker, R.V., et al., *Fibrocystin/Polyductin releases a C-terminal fragment that*
1000 *translocates into mitochondria and suppresses cystogenesis.* Nat Commun, 2023.
1001 **14**(1): p. 6513.
1002 87. Chong, Y.C., et al., *Bifurcating action of Smoothened in Hedgehog signaling is*
1003 *mediated by Dlg5*. Genes Dev, 2015. **29**(3): p. 262-76.
1004 88. Marquez, J., et al., *DLG5 variants are associated with multiple congenital anomalies*
1005 *including ciliopathy phenotypes*. J Med Genet, 2021. **58**(7): p. 453-464.
1006 89. Lu, Q., et al., *Early steps in primary cilium assembly require EHD1/EHD3-dependent*
1007 *ciliary vesicle formation.* Nat Cell Biol, 2015. **17**(3): p. 228-240.
1008 90. Doench, J.G., et al., *Optimized sgRNA design to maximize activity and minimize off-*
1009 *target effects of CRISPR-Cas9.* Nat Biotechnol, 2016. **34**(2): p. 184-191.
1010 91. Ran, F.A., et al., *Genome engineering using the CRISPR-Cas9 system.* Nat Protoc,
1011 2013. **8**(11): p. 2281-2308.
1012 92. Wu, H., et al., *Subcellular targeting and cytoskeletal attachment of SAP97 to the*
1013 *epithelial lateral membrane.* J Cell Biol, 1998. **111**: p. 2365-76.
1014 93. Campeau, E., et al., *A versatile viral system for expression and depletion of proteins*
1015 *in mammalian cells*. PLoS One, 2009. **4**(8): p. e6529.

1016 94. Tyanova, S., T. Temu, and J. Cox, *The MaxQuant computational platform for mass*
1017 *spectrometry-based shotgun proteomics.* Nat Protoc, 2016. **11**(12): p. 2301-2319.
1018 95. Alexa, A. and J. Rahnenfuhrer. *topGO: Enrichment Analysis for Gene Ontology*. R
1019 package version 2.54.0 2023; https://bioconductor.org/packages/topGO].
1020 96. Hua, K. and R.J. Ferland, *Fixation methods can differentially affect ciliary protein*
1021 *immunolabeling.* Cilia, 2017. **6**: p. 5.
1022 97. He, K., et al., *Axoneme polyglutamylation regulated by Joubert syndrome protein*
1023 *ARL13B controls ciliary targeting of signaling molecules.* Nat Commun, 2018. **9**(1):
1024 p. 3310.
1025 98. Goncalves, A.B., et al., *CEP78 functions downstream of CEP350 to control*
1026 *biogenesis of primary cilia by negatively regulating CP110 levels.* Elife, 2021. **10**.
1027 99. Schindelin, J., et al., *Fiji: an open-source platform for biological-image analysis.* Nat
1028 Methods, 2012. **9**(7): p. 676-82.
1029 100. Evans, R., et al., *Protein complex prediction with AlphaFold-Multimer.* 2022.
1030 101. Gaeggeler, H.P., et al., *Mineralocorticoid versus glucocorticoid receptor occupancy*
1031 *mediating aldosterone-stimulated sodium transport in a novel renal cell line.* J Am
1032 Soc Nephrol, 2005. **16**(4): p. 878-91.

1033

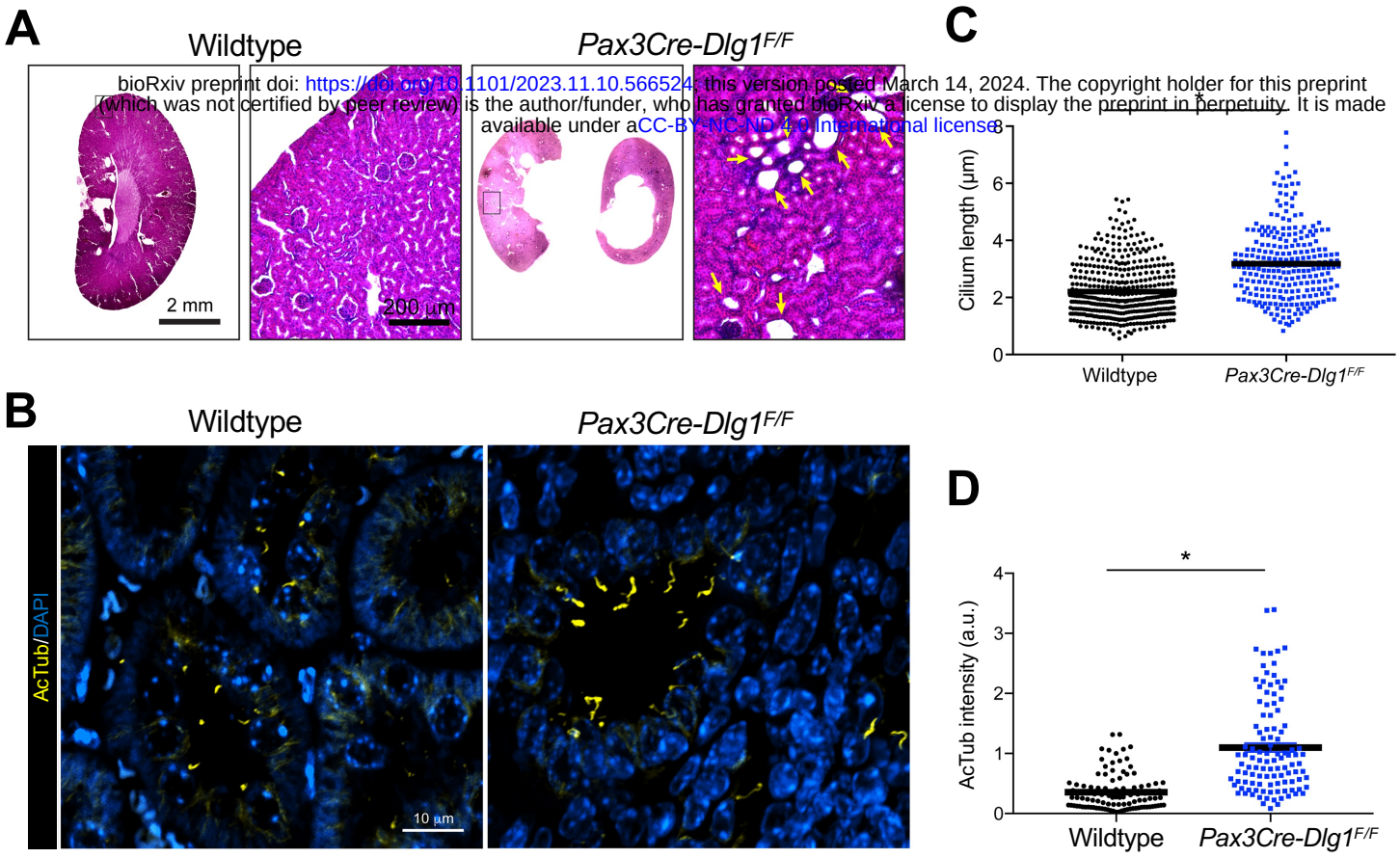

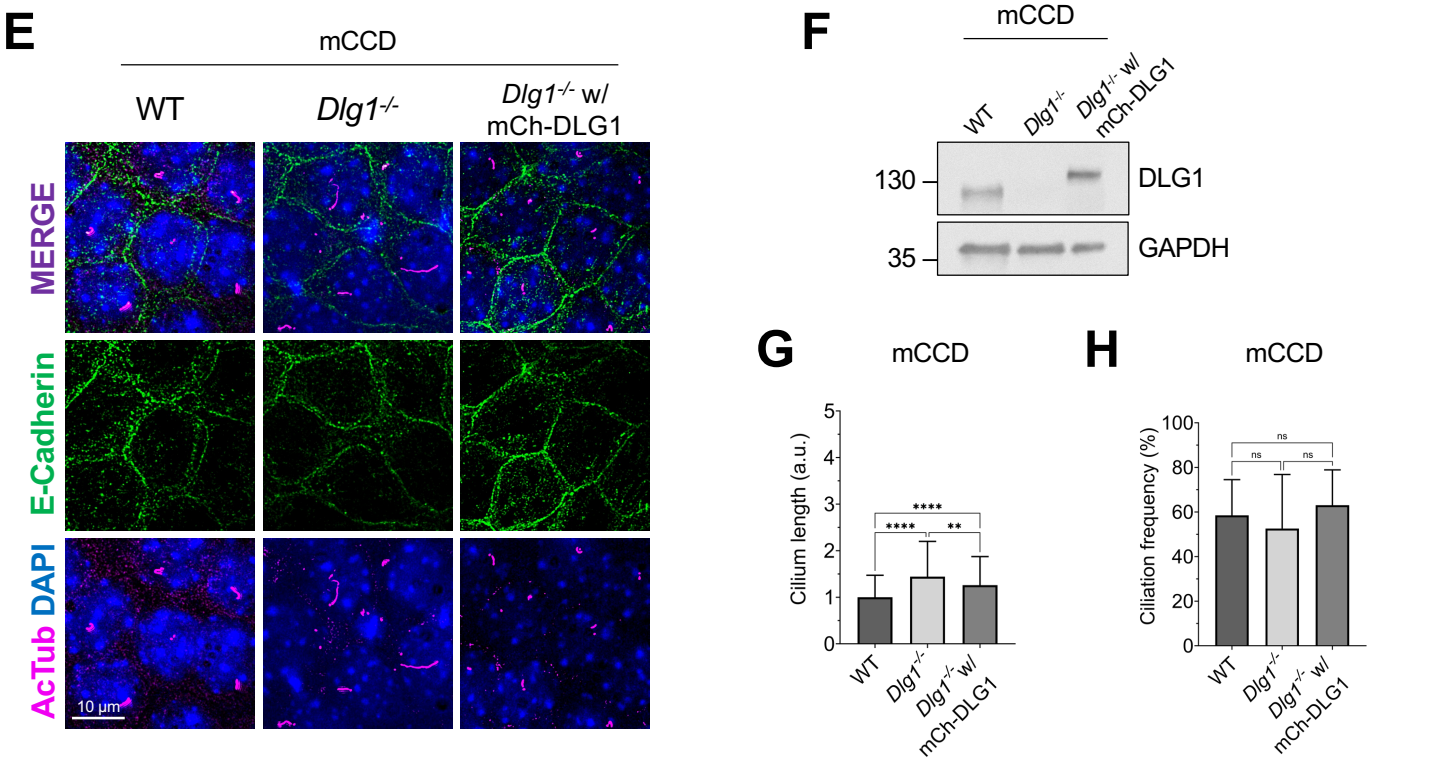

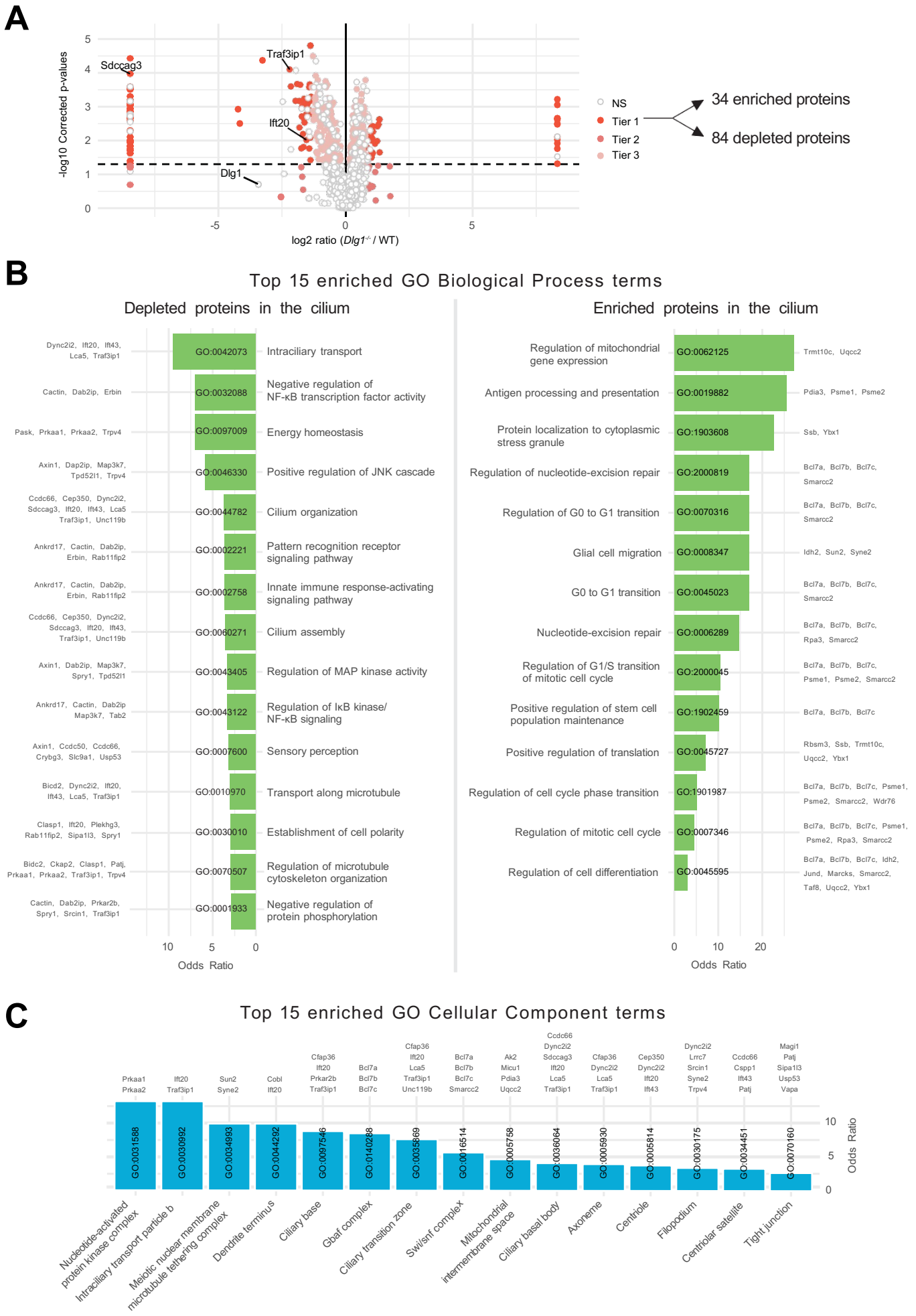
A
-log10 Corrected p-values
log2 ratio (Dlg1-/- / WT)
Sdccag3
Traf3ip1
Ift20
Dlg1
NS
Tier 1
Tier 2
Tier 3
34 enriched proteins
84 depleted proteins
B
Top 15 enriched GO Biological Process terms
Depleted proteins in the cilium
Enriched proteins in the cilium
Odds Ratio
GO:0042073 Intraciliary transport
GO:0032088 Negative regulation of NF-κB transcription factor activity
GO:0097009 Energy homeostasis
GO:0046330 Positive regulation of JNK cascade
GO:0044782 Cilium organization
GO:0002221 Pattern recognition receptor signaling pathway
GO:0002758 Innate immune response-activating signaling pathway
GO:0060271 Cilium assembly
GO:0043405 Regulation of MAP kinase activity
GO:0043122 Regulation of IκB kinase/ NF-κB signaling
GO:0007600 Sensory perception
GO:0010970 Transport along microtubule
GO:0030010 Establishment of cell polarity
GO:0070507 Regulation of microtubule cytoskeleton organization
GO:0001933 Negative regulation of protein phosphorylation
Regulation of mitochondrial gene expression
Antigen processing and presentation
Protein localization to cytoplasmic stress granule
Regulation of nucleotide-excision repair
Regulation of G0 to G1 transition
Glial cell migration
G0 to G1 transition
Nucleotide-excision repair
Regulation of G1/S transition of mitotic cell cycle
Positive regulation of stem cell population maintenance
Positive regulation of translation
Regulation of cell cycle phase transition
Regulation of mitotic cell cycle
Regulation of cell differentiation
GO:0062125
GO:0019882
GO:1903608
GO:2000819
GO:0070316
GO:0008347
GO:0045023
GO:0006289
GO:2000045
GO:1902459
GO:0045727
GO:1901987
GO:0007346
GO:0045595
C
Top 15 enriched GO Cellular Component terms
Odds Ratio
GO:0031588 Nucleotide-activated protein kinase complex
GO:0030992 Intraciliary transport particle b
GO:0034993 Meiotic nuclear membrane microtubule tethering complex
GO:0044292 Dendrite terminus
GO:0097546 Ciliary base
GO:0140288 Gbaf complex
GO:0035869 Ciliary transition zone
GO:0016514 Swi/snf complex
GO:0005758 Mitochondrial intermembrane space
GO:0036064 Ciliary basal body
GO:0005930 Axoneme
GO:0005814 Centriole
GO:0030175 Filopodium
GO:0034451 Centriolar satellite
GO:0070160 Tight junction

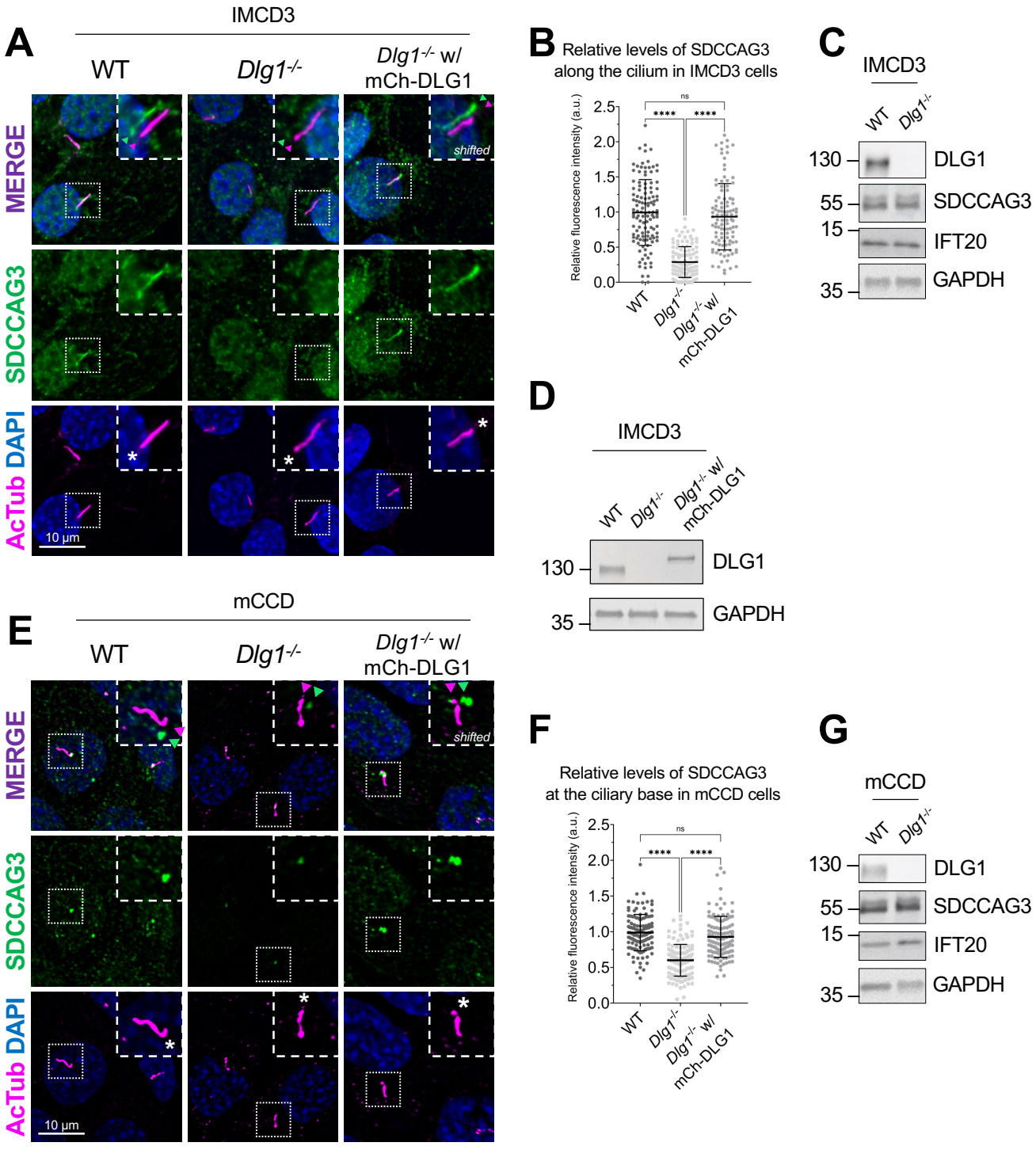
A
IMCD3
WT
Dlg1-/-
Dlg1-/- w/ mCh-DLG1
MERGE
SDCCAG3
AcTub DAPI
shifted
10 µm
B
Relative levels of SDCCAG3 along the cilium in IMCD3 cells
Relative fluorescence intensity (a.u.)
ns
****
****
WT
Dlg1-/-
Dlg1-/- w/ mCh-DLG1
C
IMCD3
WT
Dlg1-/-
130
55
15
35
DLG1
SDCCAG3
IFT20
GAPDH
D
IMCD3
WT
Dlg1-/-
Dlg1-/- w/ mCh-DLG1
130
35
DLG1
GAPDH
E
mCCD
WT
Dlg1-/-
Dlg1-/- w/ mCh-DLG1
MERGE
SDCCAG3
AcTub DAPI
shifted
10 µm
F
Relative levels of SDCCAG3 at the ciliary base in mCCD cells
Relative fluorescence intensity (a.u.)
ns
****
****
WT
Dlg1-/-
Dlg1-/- w/ mCh-DLG1
G
mCCD
WT
Dlg1-/-
130
55
15
35
DLG1
SDCCAG3
IFT20
GAPDH

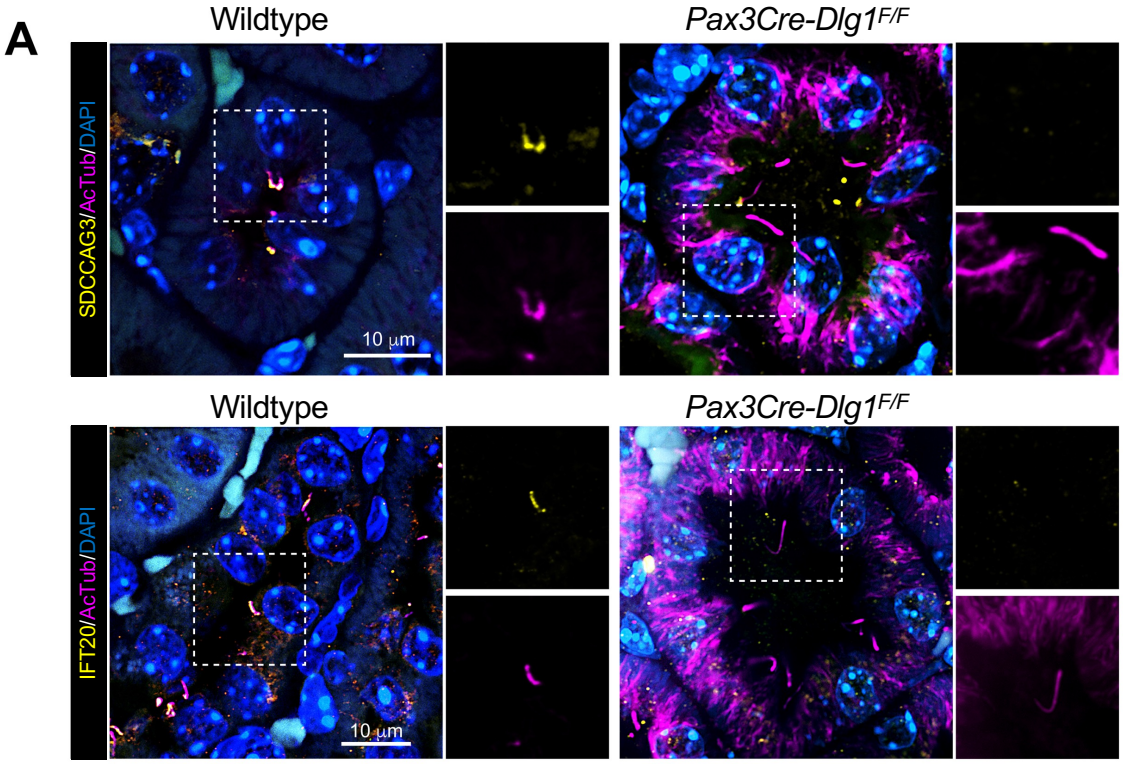
A
Wildtype
Pax3Cre-Dlg1F/F
SDCCAG3/AcTub/DAPI
10 μm
Wildtype
Pax3Cre-Dlg1F/F
IFT20/AcTub/DAPI
10 μm

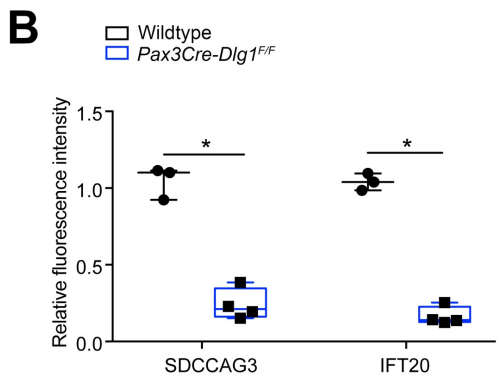
B
Wildtype
Pax3Cre-Dlg1F/F
Relative fluorescence intensity
1.5
1.0
0.5
0.0
*
*
SDCCAG3
IFT20

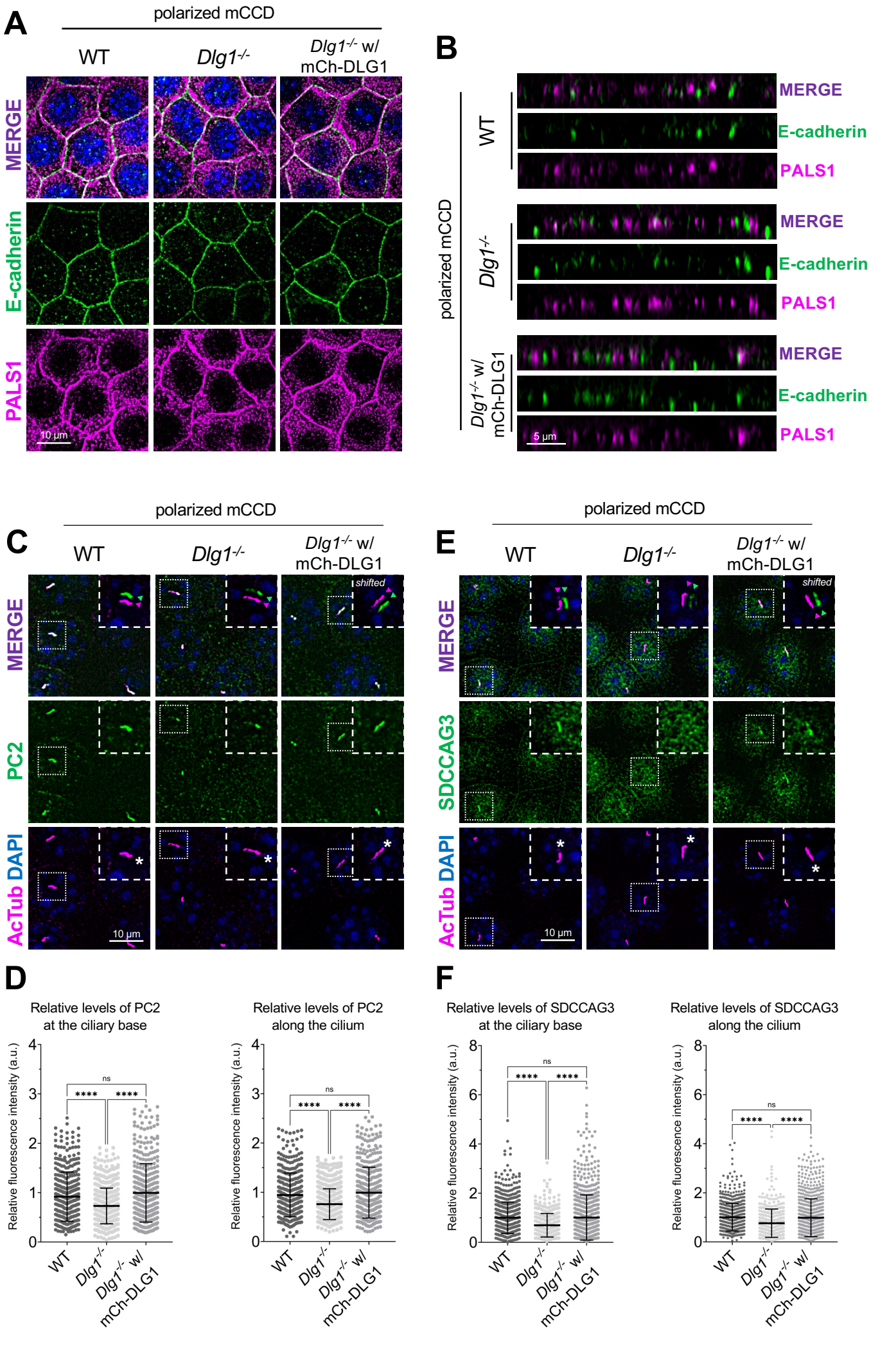
A
polarized mCCD
WT
Dlg1-/-
Dlg1-/- w/ mCh-DLG1
MERGE
E-cadherin
PALS1
10 μm
B
polarized mCCD
WT
Dlg1-/-
Dlg1-/- w/ mCh-DLG1
MERGE
E-cadherin
PALS1
5 μm
C
polarized mCCD
WT
Dlg1-/-
Dlg1-/- w/ mCh-DLG1
shifted
MERGE
PC2
AcTub DAPI
10 μm
E
polarized mCCD
WT
Dlg1-/-
Dlg1-/- w/ mCh-DLG1
shifted
MERGE
SDCCAG3
AcTub DAPI
10 μm
D
Relative levels of PC2 at the ciliary base
Relative levels of PC2 along the cilium
Relative fluorescence intensity (a.u.)
ns
****
WT
Dlg1-/-
Dlg1-/- w/ mCh-DLG1
F
Relative levels of SDCCAG3 at the ciliary base
Relative levels of SDCCAG3 along the cilium
Relative fluorescence intensity (a.u.)
ns
****
WT
Dlg1-/-
Dlg1-/- w/ mCh-DLG1

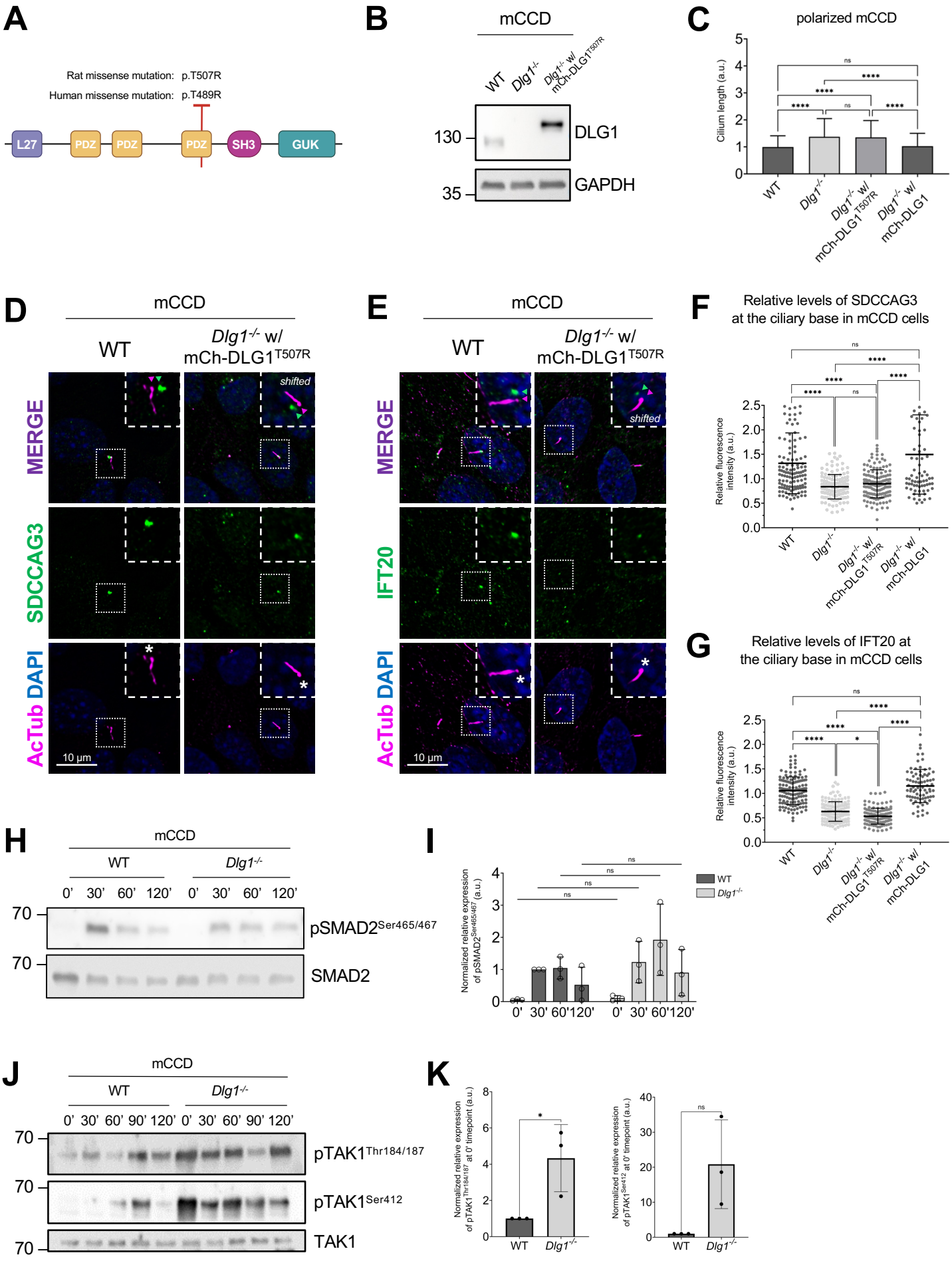
A
Rat missense mutation: p.T507R
Human missense mutation: p.T489R
L27
PDZ
PDZ
PDZ
SH3
GUK
B
mCCD
WT
Dlg1-/-
Dlg1-/- w/ mCh-DLG1T507R
130
DLG1
35
GAPDH
C
polarized mCCD
Cilium length (a.u.)
WT
Dlg1-/-
Dlg1-/- w/ mCh-DLG1T507R
Dlg1-/- w/ mCh-DLG1
D
mCCD
WT
Dlg1-/- w/ mCh-DLG1T507R
MERGE
SDCCAG3
AcTub DAPI
shifted
10 µm
E
mCCD
WT
Dlg1-/- w/ mCh-DLG1T507R
MERGE
IFT20
AcTub DAPI
shifted
10 µm
F
Relative levels of SDCCAG3 at the ciliary base in mCCD cells
Relative fluorescence intensity (a.u.)
G
Relative levels of IFT20 at the ciliary base in mCCD cells
Relative fluorescence intensity (a.u.)
H
mCCD
WT
Dlg1-/-
0' 30' 60' 120' 0' 30' 60' 120'
70
pSMAD2Ser465/467
70
SMAD2
I
Normalized relative expression of pSMAD2Ser465/467 (a.u.)
WT
Dlg1-/-
0' 30' 60'120' 0' 30' 60'120'
J
mCCD
WT
Dlg1-/-
0' 30' 60' 90' 120' 0' 30' 60' 90' 120'
70
pTAK1Thr184/187
70
pTAK1Ser412
70
TAK1
K
Normalized relative expression of pTAK1Thr184/187 at 0' timepoint (a.u.)
Normalized relative expression of pTAK1Ser412 at 0' timepoint (a.u.)
WT
Dlg1-/-